Stability and aggregation propensities of ALS-associated human superoxide dismutase mutants

by

Ming Sze Tong

A thesis
presented to the University of Waterloo
in fulfilment of the
thesis requirement for the degree of
Master of Science
in
Chemistry

Waterloo, Ontario, Canada, 2010

Author's Declaration

I hereby declare that I am the sole author of this thesis. This is a true copy of the thesis, including any required final revisions, as accepted by my examiners.

I understand that my thesis may be made electronically available to the public.

Abstract

Amyotrophic lateral sclerosis (ALS) is the most common motor neuron disease and is characterized by progressive paralysis leading to death, typically, within 3-5 years of the onset of symptoms. The majority of ALS cases are sporadic with no known causative agent; however, 5-10% of ALS cases are genetically inherited and termed familial ALS (fALS). Approximately, 15-20% of these fALS cases have been linked to mutations in the gene encoding human Cu/Zn superoxide dismutase (hSOD). To date, over 140 hSOD mutations have been discovered. The mechanisms by which mutant hSOD confers toxicity in fALS patients are still unknown. However, there is growing evidence that ALS is a type of protein conformational disease whereby cell damage or death is caused by the accumulation of protein aggregates in the cell. It is hypothesized that mutations destabilise hSOD and increase its propensity to aggregate. There is some controversy as to which hSOD species contributes to aggregation. Many believe that only apo or mismetallated forms of hSOD are able to aggregate. Due to the abundance of fully metallated or holo hSOD in the cell, we hypothesize that holo hSOD can also lead to aggregation. Holo dimer interface mutants A4S, A4T and I113T as well as G41D were found to be destabilized compared to holo pseudo wildtype (pWT) while zinc binding mutant H80R was shown to form fragments via an unknown mechanism. Holo dimer interface mutants A4S and A4T were also shown to have an increased propensity to aggregate compared to pWT, which correlates to their decreased stability as well a short disease durations.

Acknowledgements

First and foremost, I would like to thank Dr. E. M. Meiering for giving me the opportunity to pursue the research presented in this thesis. I would also like to thank her for all her guidance and insight, both academically and on life.

I would also like to thank the members of the Meiering laboratory, past and present, for all their help and support. I would especially like to thank Gracie Hwang, Dr. Jessica Rumfeldt, Helen Stubbs and Kenrick Vassall.

Last but not least, I would like to thank my parents, Tong Chap Thy and Teoh Teik Gek, for supporting me throughout my life, through many years of formal education and for all the sacrifices they have made for me to be where I am today. And to my partner, Andi, I thank you for your love and support, and your unending faith in me.

Dedication

For papa & mama

and katze

Table of Contents

List of Tables

List of Figures

List of Abbreviations

AD .... Alzheimer's disease

ALS ....amyotrophic lateral sclerosis

apo hSOD .... metal free form of human copper zinc superoxide dismutase

BSA ....bovine serum albumin

C_p .... specific heat capacity

DLS ....dynamic light scattering

DSC .... differential scanning calorimetry

EDTA ....ethylenediaminetetraacetic acid

fALS .... familial amyotrophic lateral sclerosis

HD ....Huntington's disease

HEPES ....4-(2-hydroxyethyl)-1-piperazineethanesulfonic acid

Holo hSOD .... fully metallated form of human copper zinc superoxide dismutase

hSOD ....human copper zinc superoxide dismutase

IPTG ....isopropyl beta-D-thiogalactopyranoside

ICP-AES .... inductively-coupled plasma atomic emission spectroscopy

ITC ....isothermal titration calorimetry

kcal .... kilocalorie

K_d .... dissociation constant

LB ....luria broth

MBR.. metal binding region

OS ....osmotic shock

PCD.. protein conformational disease

PD .... Parkinson's disease

pWT .... pseudo-wildtype human Cu/Zn superoxide dismutase

NMR .... nuclear magnetic resonance

N_2 .... native dimer

R.. universal gas constant, 1.986 cal/mol/K

sALS .... sporadic amyotrophic lateral sclerosis

SDS-PAGE ....sodium dodecyl sulphate polyacrylamide gel electrophoresis

SOC... super optimal broth with catabolite repression

SOD..superoxide dismutase

TSE .... transmissible spongiform encephalopathies

T_m...temperature where the fraction of unfolded protein is one half

Tris-HCl... tris (hydroxymethyl) aminomethane hydrochloride

U..unfolded state

2TY .... rich tryptone and yeast extract medium

β .... $\frac{\Delta H_{vH}}{\Delta H_{cal}}$ x molecular weight of the hSOD dimer

ΔC_p .... change in specific heat capacity upon unfolding

ΔG ....difference in Gibb's free energy between two stable states

Δh... change in specific heat capacity unpon unfolding

ΔH ....change in enthalpy upon unfolding

ΔH_{cal} ....calorimetric enthalpy of unfolding

ΔH_{vH} .... van't Hoff enthalpy of unfolding

ΔS .... change in entropy unpon unfolding

$\Delta\Delta G$ ....difference in ΔG between mutant and pWT

$\Delta\Delta H$... difference in ΔH between mutant and pWT

$\Delta\Delta S$..difference in ΔS between mutant and pW

Chapter 1 General introduction

1.1   Protein conformational diseases

Protein conformational diseases (PCDs) are a group of diseases that involve the conversion of a specific protein or proteins from a native fold to a non-native fold that eventually leads to the formation cytotoxic oligomers or aggregates (1). As many as forty types of PCDs have been discovered to date (2,3). The different proteins involved in PCDs do not share any similarities in primary sequence or native structure; however, they share a vital characteristic whereby the proteins involved have the ability to adopt certain conformational changes that enable the formation of insoluble aggregates (3). Protein folding is a complicated process that includes many opportunities for side reactions that can lead to aggregate-formation (4). The majority of cases of PCDs are sporadic with no known causative agents. However, a small portion of PCDs are associated with mutations in their associated proteins. These familial forms of PCDs may provide some insight to the pathogenesis of the diseases. The mutations that occur in the disease associated proteins tend to be dominantly inherited and are usually associated with earlier disease onset (5), implying that these mutations possess some characteristics that confer increased toxicity.

Like many neurodegenerative diseases, such as Alzheimer's disease (AD), Parkinson's disease (PD), Huntington's disease (HD) and transmissible spongiform encephalopathies (TSE), amyotrophic lateral sclerosis (ALS) has been proposed to be a PCD (2). However, unlike these diseases, ALS is not an amyloid disease. Amyloid diseases are characterised by positive Congo red staining with green-gold birefringence when viewed under polarized light (6-8) and amyloid deposits with rigid unbranched fibrils with diameters of 5-13 nm and lengths of 0.1-1.6 μm

(7,9,10). On the other hand, deposits found in ALS patients do not bind Congo red (11) and contain filamentous as well as granule-coated fibrils (12-14).

1.2   Amyotrophic lateral sclerosis

Amyotrophic lateral sclerosis (ALS) is the most common motor neuron disease with a prevalence of 1.5-2.5 in 100,000 individuals per year (15). To date, no cure has been found for ALS and ALS treatment has only been able to slightly delay disease progression (16,17). Amyotrophic lateral sclerosis is also referred to as Charcot's disease, after Jean-Martin Charcot who characterized the disease over 130 years ago, and more commonly as Lou Gehrig's disease, after a famous American baseball player who was stricken by the disease in the late 1930s (18,19). Amyotrophic lateral sclerosis is a late onset disease with an average onset age of 46 years (range 24-72) and is usually fatal within 3-5 years (range 0.3-20 years) of the onset of symptoms (20). Early symptoms of ALS usually are weakness in the arms and legs which progressively degenerates, inevitably leading to paralysis and death, usually due to respiratory failure. There are also cases of bulbar onset which then extends outwards. The disease selectively targets the motor neurons in the spinal cord, brain stem and cortex which usually leave the patients' intellect unaffected.

The majority of ALS cases have no known causative agents and are termed sporadic ALS (sALS). However, a small percentage of ALS cases, about 5-10%, are genetically inherited and termed familial ALS (fALS). In 1993, Rosen *et al.* discovered a genetic link between a subset of fALS cases and mutations in the *sod1* gene (21), which codes for human Cu/Zn superoxide dismutase (hSOD). Since then, over 140 fALS linked hSOD mutations, representing approximately 20% of all fALS cases (19), have been discovered (database containing hSOD

mutations found at http://alsod.iop.kcl.ac.uk/Als/index.aspx). Although hSOD mutations are associated to a small fraction of all ALS cases, it is currently the most widely studied and major known cause of the disease. Mutations in *sod1* have also been implicated in ~1% of sALS cases (22). In addition, both hSOD mutant-mediated fALS and sALS display the same symptoms and are clinically identical, suggesting a similar disease mechanism (20,23). By studying hSOD, it may be possible to elucidate the mechanism of pathogenesis and, ultimately, shed more light on this enigmatic disease.

1.3 Human Cu/Zn Superoxide Dismutase

Superoxide dismutase (SOD) is an antioxidant enzyme that protects cells from the harmful effects of superoxide, a reactive oxygen species, and is ubiquitously found in all aerobic organisms (24). In eukaryotes, it is found in the cytosol, nucleus, peroxisomes and mitochondrial intermembrane space (19). The human Cu/Zn superoxide dismutase (hSOD) is encoded in the *sod1* gene located on the long arm of chromosome 21, more specifically at 21q22 (25,26). It is a single copy gene spanning 11 kilobases and contains five exons and four introns.

1.3.1 Structure and function

Human Cu/Zn superoxide dismutase is a very stable homodimeric enzyme. The homodimer is 32 kDa in size and each monomer consists of 153 amino acids. Each monomer is composed of an 8-stranded Greek key β-barrel. The eight β-strands are antiparallel and are joined by loops (27). Each monomer also contains an active site that preferentially and very tightly binds one Cu^{2+} and one Zn^{2+} (Figure 1.1) (28). The active site on the surface of the β-barrel and is enclosed by loop 4, which is the zinc binding loop that extends into the dimer interface, and loop 7, which is the electrostatic loop. Each hSOD monomer has four cysteines; Cys-57 and Cys-146

form a conserved intramolecular disulfide bond while Cys-6 and Cys-111 are free cysteines (28). The structure of the enzyme as well as the active site residues are highly conserved (19,27). Figure 1.1 is a representation of the crystal structure of pseudo wildtype (pWT) hSOD (Section 2.1.1) with the intramolecular disulfide bonds and metals shown along with a schematic illustrating the Greek key motif of hSOD. pWT is a C6S/C111A double mutant that removes the 2 free cysteines present in hSOD.
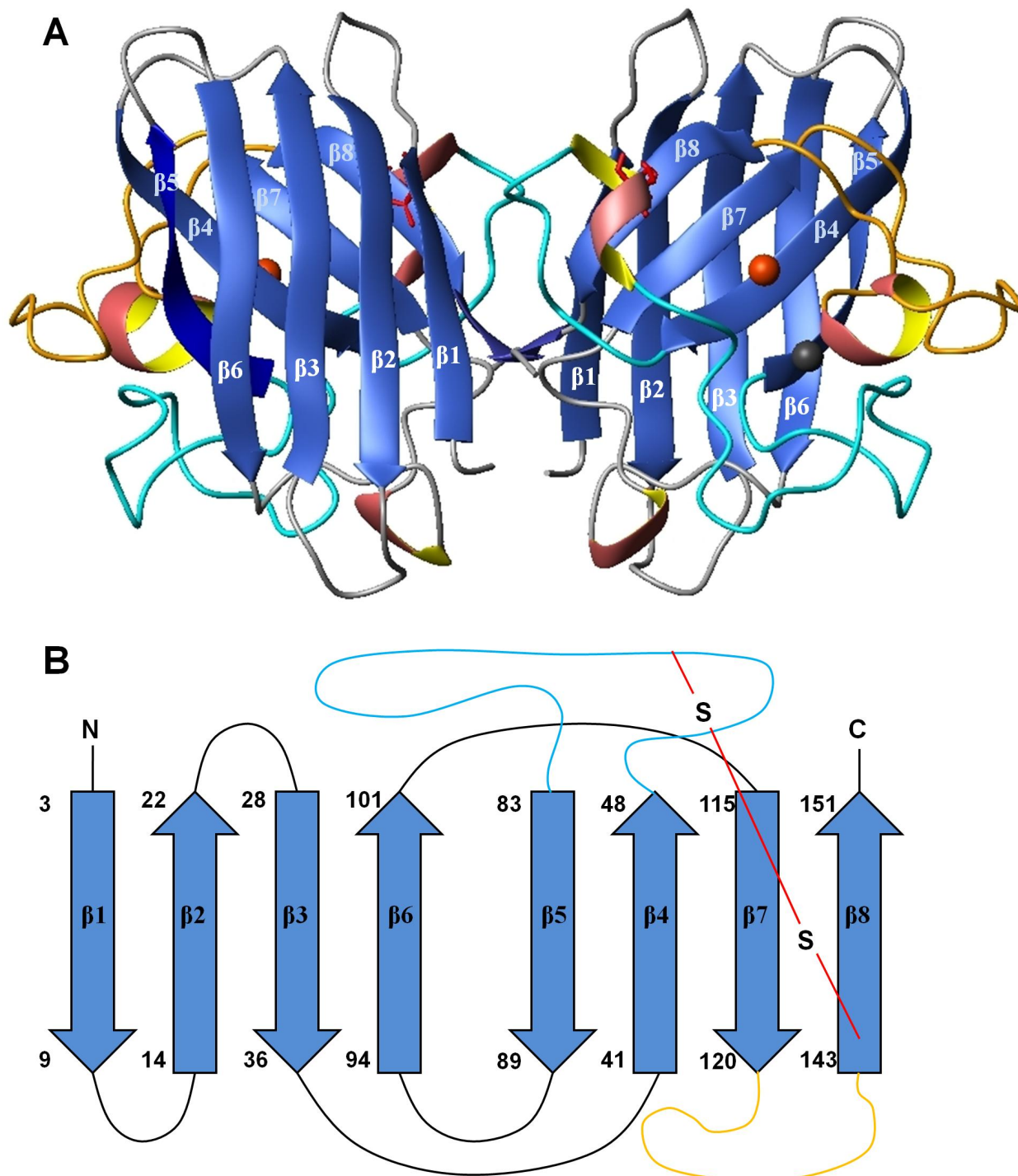
Figure 1.1 A ribbon representation of crystal structure (A) and schematic (B) of the hSOD dimer. (A) Prepared using MolMol (29) and PDB coordinates 1SOS (30). The eight β-strands are in blue while the three α-helices are in pink and yellow. Each monomer contains a Zn^{2+} and a Cu^{2+} ion depicted as black and orange spheres, respectively. In both figures, the intramolecular disulfide bond is shown in red while the zinc and electrostatic loops are in cyan and yellow, respectively.

Both metals in hSOD are important for the structural stability of the active site. The copper ion is an essential cofactor in hSOD catalysis and is cyclically oxidized and reduced during catalysis. Human Cu/Zn superoxide dismutase catalyzes the dismutation of two superoxide molecules to dioxygen and hydrogen peroxide (Reactions 1-3, below) (19). The catalysis begins with the reduction of the cupric ion by the first molecule of superoxide to produce molecular oxygen (Reaction 1) (19). The second superoxide molecule then reoxidizes the cuprous ion to produce hydrogen peroxide (Reaction 2) (19). Superoxide dismutase is among the fastest enzymes known with a rate constant of ~2 x 10^9 $M^{-1}s^{-1}$ (31).

$$O_2^- + Cu^{2+}ZnSOD \rightarrow O_2 + Cu^+ZnSOD \qquad \text{Reaction 1}$$

$$O_2^- + 2 H^+ + Cu^+ZnSOD \rightarrow H_2O_2 + Cu^{2+}ZnSOD \qquad \text{Reaction 2}$$

Overall reaction

$$2O_2^- + 2 H^+ \rightarrow O_2 + H_2O_2 \qquad \text{Reaction 3}$$
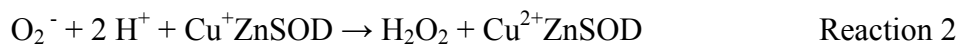
1.4 Familial ALS-associated hSOD mutations

Of the 145 *sod1* gene mutations linked to ALS, at least 117 are single amino acid substitutions at one of 74 different residues (shown in Table 1.1) (mutation list obtained from an online database http://alsod.iop.kcl.ac.uk/Als/index.aspx). Other *sod1* mutations include deletions or insertions, frameshift mutations and truncations (not indicated in Table 1.1) (19,32). All known *sod1* mutations are dominantly inherited except for D90A which exhibits variable inheritance (33-35). Although mutations are scattered throughout the protein, some of the mutations can be categorized into two distinct groups: metal binding region (MBR) mutants and dimer interface mutants. Metal binding region mutants are mutations that occur at the metal coordinating residues as well as residues in the electrostatic and zinc loops. These affect the

metal binding ability of the protein, and are expected to result in lower enzymatic activity (19). Dimer interface mutants, on the other hand, are mutations that occur in and around the dimer interface and may affect the stability of the protein. To date, no clear trends have been identified among the different types of hSOD mutations. However, a recent computational study has proposed that nearly all mutations, regardless of their position, decrease dimer stability and/or dissociation (36).

Table 1.1 The amino acid sequence of hSOD along with fALS-associated substitution mutations. The mutations are listed in red. Boxes shaded blue indicate residues in β-strands. The circles above specific residues denote metal coordinating residues where the copper and zinc are represented by yellow and black circles, respectively (mutation list obtained from an online database http://alsod.iop.kcl.ac.uk/Als/index.aspx).

1	2	3	4	5	6	7	8	9	10	11	12	13	14	15	16	17	18	19	20
A	T	K	A	V	C	V	L	K	G	D	G	P	V	Q	G	I	I	N	F
			S T V	L	F G	E	Q V		R V		R		G M		A S			S	C

21	22	23	24	25	26	27	28	29	30	31	32	33	34	35	36	37	38	39	40
E	Q	K	E	S	N	G	P	V	K	V	W	G	S	I	K	G	L	T	E
K G	L						A									R	R V		G

41	42	43	44	45	46	47	48	49	50	51	52	53	54	55	56	57	58	59	60
G	L	H	G	F	H	V	H	E	F	G	D	N	T	A	G	C	T	S	A
D S		R		C	R	A F	Q R	K					R			R		I	

61	62	63	64	65	66	67	68	69	70	71	72	73	74	75	76	77	78	79	80‡
G	P	H	F	N	P	L	S	R	K	H	G	G	P	K	D	E	E	R	H
			S	A	R						C S				V Y				R

81	82	83	84	85	86	87	88	89	90	91	92	93*	94	95	96	97	98	99	100
V	G	D	L	G	N	V	T	A	D	K	D	G	V	A	D	V	S	I	E
			F V	R S	D I K S	A M		T V	A V			A C D R		T V	N V	L M		V	K G

101	102	103	104	105	106	107	108	109	110	111	112	113	114	115	116	117	118	119	120
D	S	V	I	S	L	S	G	D	H	C	I	I	G	R	T	L	V	V	H
G H N Y			F	L	F V		V	Y			Y	M T	F T	A	G	R	V	L	

121	122	123	124	125	126	127	128	129	130	131	132	133	134	135	136	137	138	139	140
E	K	A	D	D	L	G	K	G	G	N	E	E	S	T	K	T	G	N	A
			G V	H	S							V	N					D H K	G

141	142	143	144	145	146	147	148	149	150	151	152	153
G	S	R	L	A	C	G	V	I	G	I	A	Q
E			F S	G T	R	D R	G I	T		S T		

* G93 has an additional two mutations not listed in the table; G93S and G93V
‡ H80R is an sALS-associated mutant, no fALS cases of H80R have been found

8

1.5   Human SOD involvement in ALS pathology

Due to the role of superoxide dismutase as an antioxidant enzyme, it was initially thought that hSOD toxicity was due to a loss or decrease in enzymatic activity (23). However, many studies indicate that hSOD toxicity is caused by a toxic gain-of-function as opposed to a loss of function. For example, transgenic mice expressing fALS-associated hSOD mutants show ALS-like symptoms despite having elevated hSOD activity (37). More compelling evidence against the loss of function theory is the fact that hSOD knockout transgenic mice do not develop motor neuron disease and appear to have a normal lifespan (38). Other studies showed that transgenic mice coexpressing endogenous mouse SOD with fALS-associated hSOD mutants still develop ALS-like symptoms and overexpressing wild-type hSOD with mutant hSOD either did not alleviate the symptoms or accelerated disease progression (39), suggesting that cytotoxicity is due to some intrinsic property in the hSOD mutants.

Despite the strong consensus for the toxic gain-of-function theory, the specific mechanism of pathogenesis has yet to be elucidated. The two main gain-of-toxic function hypotheses, which are not mutually exclusive, are: 1) oxidative damage hypothesis and 2) protein aggregation hypothesis. The oxidative damage hypothesis proposes that ALS-associated mutations reduce the specificity of the active site, increasing the probability of harmful, non-native chemistry and the generation of free radicals. In the presence of hydrogen peroxide, mutant hSOD have been shown to generate hydroxyl radicals that can lead to oxidative damage and deactivation of the enzyme (40-42). Additionally, G93A mouse model studies found increased levels of oxygen radicals and oxidative damage in the spinal cords of the mice (43,44). HSOD can also react with peroxynitrite to produce a nitronium-like intermediate that can then nitrate tyrosine residues leading to protein damage (45). Elevated levels of nitrotyrosine have

9

been found in motor neurons of sALS and fALS patients (46) as well as ALS mice models (47,48). Despite the supporting evidence for the oxidative damage hypothesis, it is unlikely that it is the common factor causing ALS. This is due to the fact that these mechanisms require the presence of the active site copper and metal binding mutants that have decreased/no copper binding still lead to the disease. Additionally, a mice model with all four copper binding residues mutated, eliminating copper binding, nevertheless develope typical disease symptoms (49).

The protein aggregation hypothesis proposes that fALS-associated mutations increase hSOD's propensity to misfold and aggregate, and it is the aggregates that confer hSOD's cytotoxic properties. Indeed, protein misfolding and aggregation appear to be associated with the pathogenesis of many neurodegenerative diseases such as Alzheimer's disease (AD), Parkinson's disease (PD) and Huntington's disease (HD) (19). Proteinaceous inclusions from some sALS and fALS patients (50-52), transgenic mice and cell culture models of ALS have all been shown to be strongly immunoreactive to hSOD antibodies (37,39,53). In cell lines where protein folding chaperones are co-expressed with mutant hSOD, aggregate formation is reduced while cell viability increases (54), implicating that aggregates play a role in cell death. It is likely that fALS-associated hSOD mutant pathogenesis is not exclusively caused by a single mechanism; however, hSOD aggregation clearly plays a role in fALS pathology.

1.6   Research objective and outline

Our lab in focused on elucidating the mechanisms whereby ALS-associated hSOD mutations increase the propensity of hSOD to aggregate. This thesis presents biophysical analyses of fALS-associated dimer interface mutants A4S, A4T and I113T in terms of their thermal stability and propensity to aggregate as well as preliminary stability data on two other

mutants, G41D and H80R. Chapter 2 describes the introduction of various structurally and chemically diverse ALS-associated hSOD mutations to the pseudo wildtype (pWT) hSOD background using polymerase chain reaction-site directed mutagenesis. Very little biophysical data is available for many of these mutants and this has served to increase the catalogue of available mutants for analysis. In Chapter 3, the thermal stability of fALS-associated mutants A4T, A4S, I113T and G41D in the fully metallated (holo) state is determined using differential scanning calorimetry (DSC). In addition, the mechanism as well as changes in enthalpy, entropy and overall free energy of unfolding are analyzed. Preliminary characterization of the metal binding mutant H80R is also included in this chapter. Chapter 4 focuses on the *in vitro* aggregation mechanism of the holo form of the dimer interface mutants A4S and A4T. Differences in aggregation propensity of the mutants compared to pWT are considered together with thermal stability and epidemiological data to identify any correlations. The overall objective is to elucidate the factors that confer toxicity to ALS-associated hSOD mutants, such as specific characteristics of the mutants that promote aggregation, and to contribute to the collective knowledge available on the disease, which may one day aid in the discovery of a cure.

Chapter 2 Expressing recombinant fALS-associated mutants in *Escherichia coli*

2.1   Introduction

2.1.1 Pseudo wildtype hSOD

Pseudo wildtype hSOD is a C6A/C111S double mutant which replaces the free cysteines in position 6 and 111 with alanine and serine, respectively, and will be referred to as pWT. These mutations make quantitative thermodynamic analysis possible by preventing the formation of aberrant intermolecular disulfide bonds during thermal unfolding experiments, making the process reversible (28). PWT hSOD has very similar structure, activity, thermal and chemical stability as the wildtype hSOD (24,55).

2.1.2 The recombinant pHSOD1ASlacI^q vector

To enable the expression of fALS-associated mutants in *Escherichia coli*, each mutation of interest is introduced to the pHSOD1ASlacI^q vector (Figure 2.1) (31). The pHSOD1ASlacI^q vector, a derivative of the pBR322 vector (56), is 5747 bp in size and contains the gene for pWT (57) connected to a leader sequence from the SOD gene of *Photobacterium leiognathi* (58), which directs the protein to be secreted to the periplasmic space. It also contains an ampicillin resistance gene for selection and the genes for the *lac* repressor and *tac*I promoter (59) for efficient regulation of hSOD expression. The pHSOD1ASlacI^q vector was a gift from Professor R.A. Hallewell (Department of Biochemistry, Imperial College of Science, Technology and Medicine, London, UK).
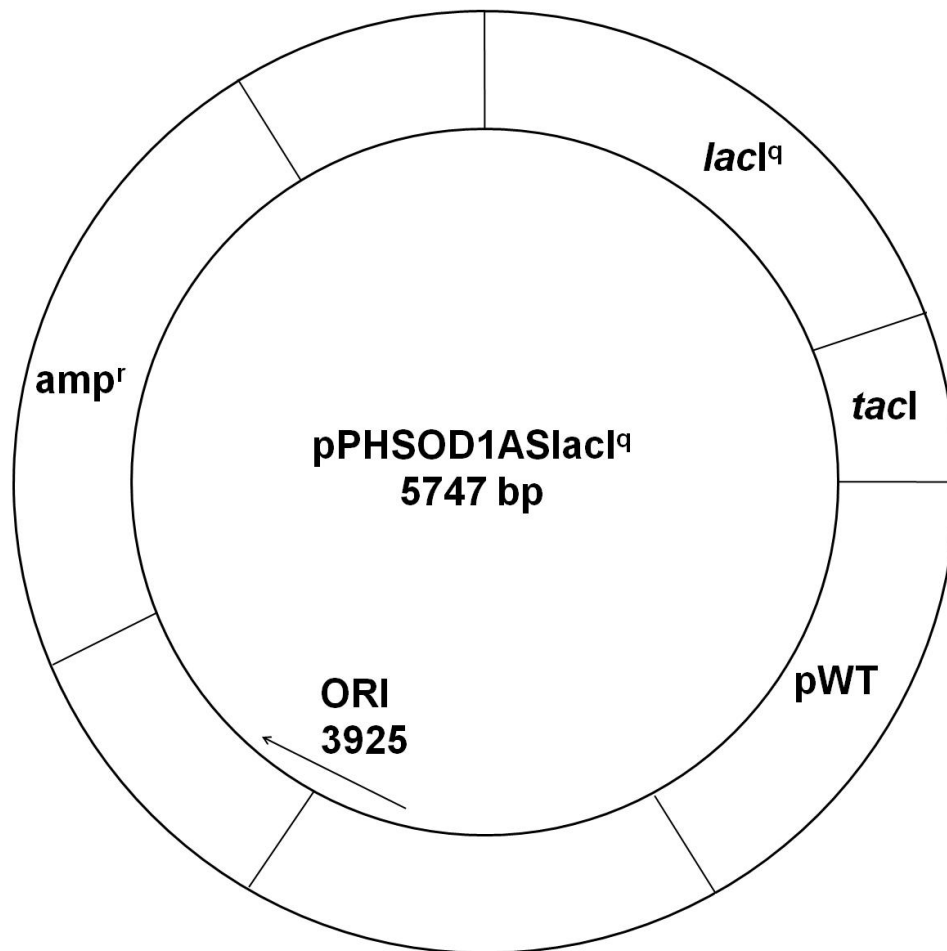
Figure 2.1 A schematic of the pPHSOD1ASlacI^q vector. The plasmid contains the gene for pWT (57) connected to a leader sequence from the SOD gene of *Photobacterium leiognathi* (58) as well as genes encoding ampicillin resistance (amp^r), the *lac* repressor (*lac*I^q) and *tac*I promoter (*tac*I) (59) (adapted from (60)).

2.1.3 Mutants of interest

To date, over 140 point mutations in hSOD have been associated with fALS. These mutations are found throughout the protein, illustrated in Table1.1. Nearly all reported mutations are dominantly inherited, with the exception of D90A which is recessively inherited (53) and a few cases expressing varying degrees of penetrance (61,62). Clearly, it is important to study these mutants and determine the properties they possess that that lead to ALS. The mutations studied in this thesis are structurally (Figure 2.2) and chemically diverse which include dimer

interface mutations (A4S, A4T, I112T, V148G, V148I), metal binding region mutations (H48R – copper binding site mutant, H80R – zinc binding site mutant) as well as mutations in the beta barrel (G37R, G41D, N86D), which also charge mutations. Table 2.1 is a summary of available patient data for the aforementioned mutations.
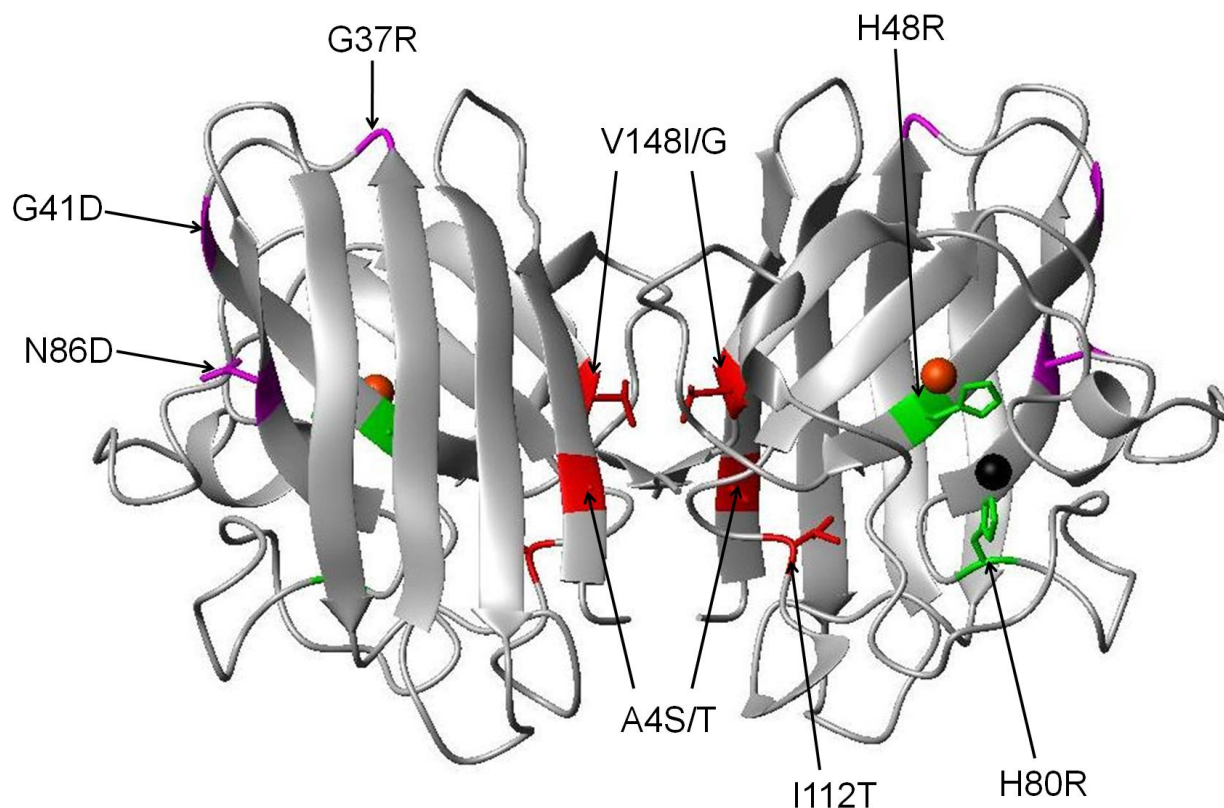
Figure 2.2 Mutation sites in hSOD associated to ALS that were studied in this thesis. Prepared using MolMol (29) and PDB coordinates 1SOS (30). Each monomer contains a Zn^{2+} and a Cu^{2+} ion depicted as black and orange spheres, respectively. Ther dimer interface, MBR and charge mutants are labelled in red, green and magenta, respectively.

Table 2.1 Summary of available patient data on mutants discussed in this thesis as well as the average values for fALS and sALS cases. The higher numbers of patients for disease onset age compared to duration are from diagnosed patients who are still alive.

Mutant	Duration in years (number of patients)	Onset in years (number of patients)	Source
A4S	>3^a (1)	34 (1)	(63)
A4T	1.5 (21)	45.3 (26)	(64)
A4V	1.2 (205)	47.7 (212)	(64)
G37R	17 (27)	36.9 (27)	(64)
G41D	14.1 (15)	45.2 (17)	(64)
H48R^b	-	-	(32)
H80R	1.5 (1)	24 (1)	(65)
N86D^b	-	-	(66)
I112T	0.9 (2)	44.0 (2)	(64)
I113T	4.3 (38)	56.3 (43)	(64)
V148G	2.1 (11)	43.1 (11)	(64)
V148I	1.7 (5)	28 (4)	(64)
fALS^c	4.0	45	(67)
sALS	2.5 (269)	58.4 (359)	(64)

^{a} Patient was still alive during study
^{b} Patient data was not reported
^{c} number of patient not provided

These mutations were introduced into the pHSOD1ASlacI^q vector via polymerase chain reaction

(PCR)-site directed mutagenesis to enable the large scale expression of the mutants required for

in depth biophysical studies.

2.2   Methods

2.2.1 Production of recombinant fALS-associated hSOD plasmids using PCR-mediated site-directed mutagenesis

Plasmids encoding fALS-associated hSOD mutants were expressed in the *E. coli* strain XL1-Blue. A modification of the QuickChange® Site Directed Mutagenesis protocol (Strategene, La Jolla, CA) was used to produce the fALS-associated hSOD mutants A4S, A4T, G37R, G41D, H48R, N86D, I112T, V148G and V148I and an sALS-associated mutant H80R. The primers were designed by Joe Gaspar and Dr. Peter Stathopolous. Complementary primers for each mutant were used to introduce the desired point mutation into the pHSOD1ASlacI^q template using PCR. Each primer was designed with the desired mutation about 10-15 bases from each end of the primer and contains a minimum Guanine+Cytosine (GC) content of 40%. The primers were also designed to end in 2-3 cytosines or guanines. The melting temperature (t_m) for each primer should be above 78 °C. Table 2.2 lists the sequence modifications made for each mutant.

Table 2.2 Primer sequences for A4S, A4T, G37R, G41D, H48R, H80R, N86D, I112T and V148G/I with %GC and t_m. The first line in each primer shows the original sequence while the second line shows the primers with the point mutations introduced (**X** - point mutation, **X** - original nucleotide). t_m of the primers were provided by Sigma Genosys Canada, Oakville, Ontario.

Mutant	Primers (5'-->3')	% GC	t_m (°C)
A4S[1]	GCG GCC ACA AAG **GCC** GTT GCT GTT TTG AAG GG GCG GCC ACA AAG **TCC** GTT GCT GTT TTG AAG GG	56.25	83.2
A4T[2]	GCG GCC ACA AAG **GCC** GTT GCT GTT TTG AAG GG GCG GCC ACA AAG **ACC** GTT GCT GTT TTG AAG GG	56.25	83.2
G37R[1]	G GTG TGG GGA AGC ATT AAA **GGA** CTG ACT GAA GGC CTG CAT GG G GTG TGG GGA AGC ATT AAA **CGT** CT**C** ACT GAA GGC CTG CAT GG	54.76	86.4
G41D[1]	C ATT AAA GGA CTG ACT GAA **GGC** CTG CAT GGA TTC CAT GTT C C ATT AAA GGA CTG ACT GAA **GAC** CTG CAT GGA TTC CAT GTT C	43.90	79.8
H48R[1]	C CTG CAT GGA TTC CAT GTT **CAT** GAG TTT GGA GAT AAT ACA GC C CTG CAT GGA TTC CAT GTT **CGC** GAG TTT GGA GAT AAT ACA GC	47.62	83.1
H80R[1]	CCA AAG GAT GAA GAG AGG **CAT** GTT GGA GAC TTG GGC AAT G CCA AAG GAT GAA GAG AG**A** C**G**T GTT GGA GAC TTG GGC AAT G	50.00	83.0
N86D[1]	G CAT GTT GGA GAC TTG GGC **AAT** GTG ACC GCG GAC AAA GAT G G CAT GTT GGA GAC TTG GG**A** G**AC** GTG ACC GCG GAC AAA GAT G	56.10	87.6
I112T[2]	CA GGA GAC CAT TCC **ATC** ATT GGC CGC ACA CTA G CA GGA GAC CAT TCC **AC**C ATT GGC CGC ACA CTA G	57.58	82.4
V148G[2]	CGT TTG GCT TGT GGT **GTA** ATT GGG ATC GCC C CGT TTG GCT TGT GGT **GGA** ATT GGG ATC GCC C	58.06	84.1
V148I[2]	CGT TTG GCT TGT GGT **GTA** ATT GGG ATC GCC C CGT TTG GCT TGT GGT **ATA** ATT GGG ATC GCC C	51.61	78.9

[1]   Primers designed by Joe Gaspar
[2]   Primers designed by Dr. Peter Stathopolous

Table 2.3 lists the components required for the PCR master mix. The buffer (Buffer 1) as well as DNA polymerase mix was obtained from the Expand Long Template PCR System kit (Roche Diagnostics, Indianapolis, IN). To decrease the effects of primer dimerization, the complementary primers of each mutation were thermocycled separately in sterile PCR tubes, containing 24.25 μL of master mix and 0.25 μL of one of the two complementary primers (final

concentration 0.25 mM) for five cycles before being pooled together. Thermocycling was done

using a TC-512 Thermal Cycler (TECHNE, Cambridge) using the conditions listed in Table 2.4.

The PCR products were then treated with *Dpn*I endonuclease, which digests methylated or

hemimethylated DNA, for 1 hour in a 37 °C water bath. Since the synthesized DNA is

unmethylated, *Dpn*I will only digest the template plasmid. The recombinant plasmids were

stored at -20 °C for further analysis.

Table 2.3 PCR components for master mix. Volumes listed are for final amount after
complementary tubes are pooled together.

Component	Volume added (µL)	Final Concentration
Expand Long Template PCR System Buffer 1	5	-
pHSOD1ASlacI$_q$ template	0.5	~ 1.75 mM
dNTPs	0.5	0.25 mM each
MilliQ H$_2$O	42.5	-
Total	48.5	

Table 2.4 Conditions for thermocycling

PCR stages	Conditions
Initial denaturation	92 °C for 5 min
Pause	**Add 0.5 µL Expand Long Template PCR System DNA polymerase mix**
Initial amplification (5 cycles)	92 °C for 30 sec (denaturation) 55 °C for 1 min (annealing) 68 °C for 20 min (elongation)
Pause	**Complementary tubes pooled together**
Final amplification (15 cycles)	92 °C for 30 sec (denaturation) 55 °C for 1 min (annealing) 68 °C for 20 min (elongation)
Final elongation	68 °C for 20 min

2.2.2 Expression of recombinant plasmids

The *Dpn*I digested plasmids were transformed into XL1-Blue electrocompetent *E. coli* cells as described elsewhere (68,69). Briefly, 1 µL of *Dpn*I digested PCR product was electroporated with 40 µL of XL1-Blue *E. coli* cells and incubated in 1 mL Super Optimal broth with Catabolite repression (SOC; 0.4% (w/v) glucose, 20.0 g tryptone, 5.0 g yeast extract, 0.5 g NaCl, 0.01 M MgSO$_4$ per 1 L) at 37 °C for 1 hour. Electroporation was done using the BioRad *E. coli* Pulser (BioRad Laboratories, Inc.) for ~1 s at 1.80 kV. XL1-Blue cells have the ability to repair nicks in the mutant plasmid as well as confer tetracycline resistance. The transformed cells were plated on Luria Broth (LB) agar (10.0 g tryptone, 5.0 g yeast extract, 10.0 g NaCl, 16 g agar per 1 L) containing ampicillin (100 µg/mL) and tetracycline (10 µg/mL) to select for XL1-Blue cells that have taken up the pHSOD1ASlacI^q plasmid. Small scale protein preparations and osmotic shock (refer to Section 3.2.2.1) were performed to obtain protein to be run on a mass spectrometer. Once the protein masses have been confirmed, the HiYield^{TM} Plasmid Mini Kit (RBC BioScience) protocol for high copy number plasmid was used to purify the plasmids. These plasmids were stored at -20 °C for further use.

2.2.3 Positive electrospray ionization mass spectrometry

Positive electrospray ionization mass spectrometry was used to confirm the masses of the expressed proteins (Micromass Q-TOF Ultima). Purified samples were diluted to approximately 1 μM in 50:50 acetonitrile:water with 0.2% formic acid and injected into the mass spectrometer at a flow rate of 1μL/min, capillary voltage of 3.2 kV, cone voltage of 80 V and m/z range of 200-3000. Data analysis was done using MassLynx V4.0 (Micromass Ltd.).

2.3 Results

2.3.1 Obtaining recombinant fALS-associated hSOD plasmids using PCR-mediated site-directed mutagenesis

The PCR-mediated site-directed mutagenesis introduces desired mutations to the pHSOD1ASlacI^q template as well as amplifies the amount of recombinant mutant plasmid. The PCR products were run on 0.7% agarose gels to determine if the process was successful. Figure 2.3 is a set of PCR products containing strong, single bands for each mutant, indicating that the respective primers annealed with high specificity and that each sample was successfully amplified. The mutant I112T was never successfully amplified (data not shown) while A4T was obtained during my CHEM 494 with Dr. E. M. Meiering.
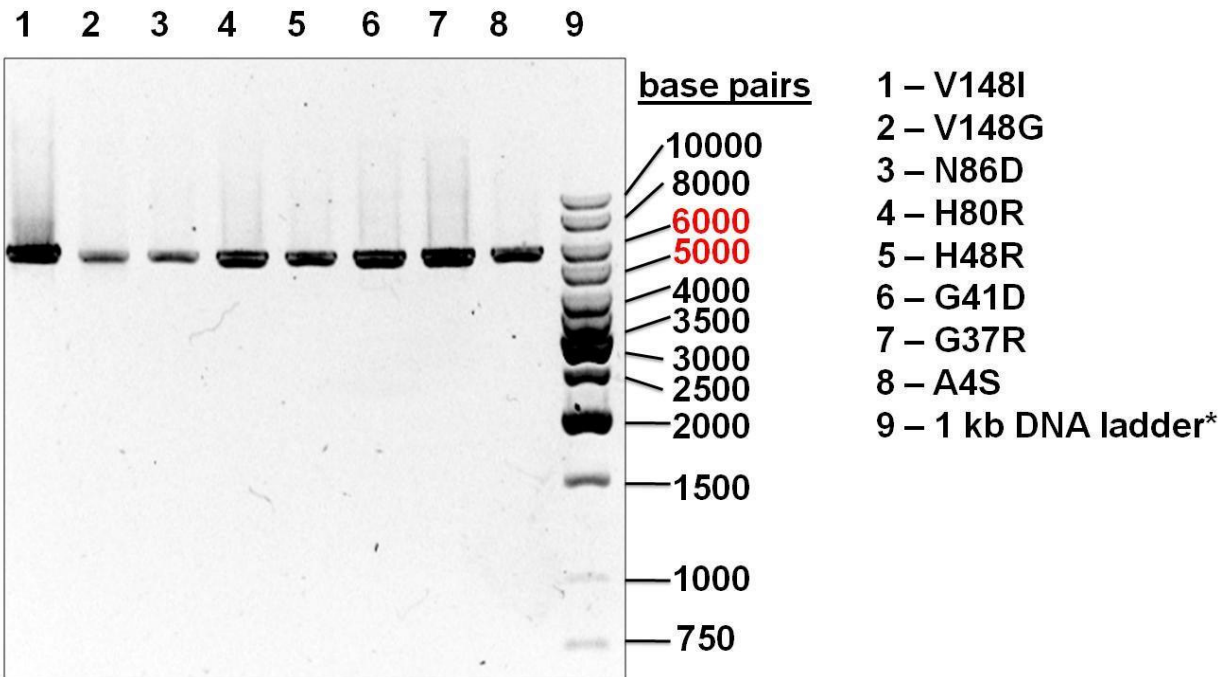
Figure 2.3 PCR products from PCR-mediated site directed mutagenesis of ALS-associated hSOD mutants. The pHSOD1ASlacI^q template is 5747 bp in size. Samples were run on a 0.7% agarose gel at a constant voltage of 100 kV. *GeneRuler™ 1 kb DNA Ladder (Fermentas Canada Inc., Burlington, Ontario)

2.3.2 Expression of recombinant hSOD

The recombinant hSOD were transformed into XL1-Blue *E. coli* and, at least, two colonies from each transformation were grown in LB broth, purified and ran on an SDS-PAGE to determine the level of expression of the PCR products (V148I transformants only produced one colony). Figure 2.4 is an SDS-PAGE of the expressed proteins from the plasmids in Figure 2.3. In this instance, all the plasmids produced hSOD and there did not appear to be a drastic decrease in protein expression for any of the samples.
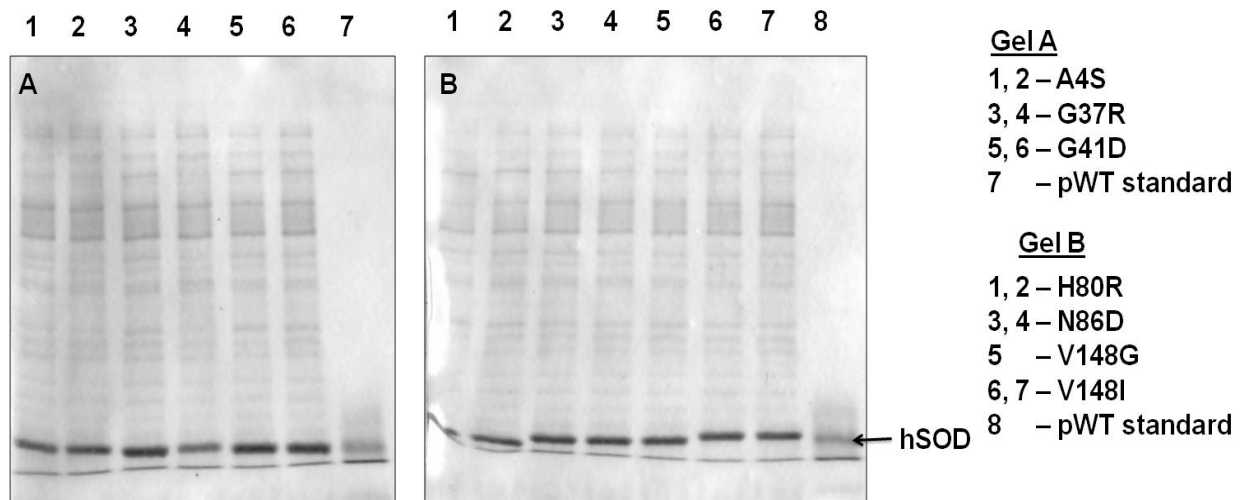
Figure 2.4 SDS-PAGE of recombinant hSOD mutants obtained expression. Purified pWT (lane A7 and B8) was used as a marker for hSOD.

2.3.3 Confirmation of recombinant hSOD mass

After it was determined that the recombinant mutants expressed hSOD, the mass of the recombinant mutants were checked via mass spectrometry to verify if the correct mutation had been introduced. Table 2.5 reports the final masses for the successfully obtained mutants and a representative mass of the unsuccessful mutants. A protein of known mass was used as a standard to obtain any offset the mass spectrometer might have. The mutants A4S, A4T, G37R, G41D, H80R, V148G and V148I were successfully obtained. Due to the similarity in mass of

N86D to pWT, the N86D plasmid was sent for sequencing which revealed that the mutagenesis was unsuccessful.

Table 2.5 Summary of recombinant hSOD masses. Listed in bold are mutants thatw ere succefully obtained.

Mutants	Apparent mass (Da)	Offset (Da)	Corrected mass (Da)	Expected mass (Da)	Mutant obtained (Y/N)
A4S	**15768.50**	**-1.99**	**15770.49**	**15770.39**	**Y**
A4T	**15783.00**	**-1.42**	**15784.42**	**15784.42**	**Y**
G37R	**15851.50**	**-1.99**	**15853.49**	**15853.52**	**Y**
G41D	**15810.00**	**-1.99**	**15811.99**	**15812.42**	**Y**
H48R	15769.00	-1.42	15770.42	15773.43	N
H80R	**15771.50**	**-1.99**	**15773.49**	**15773.43**	**Y**
N86D	15752.20	-1.99	15754.19	15755.37	N
I112T[a]	15753.80	n/a	n/a	15742.34	N
V148G	**15711.00**	**-1.42**	**15712.42**	**15712.31**	**Y**
V148I	**15767.00**	**-1.42**	**15768.42**	**15768.41**	**Y**

[a] A standard was not ran on the day I112T was checked, however, the apparent mass was sufficiently different from the expected mass to conclude that the PCR-mediated site directed mutagenesis was not successful.

2.4   Discussion

PCR-mediated site directed mutagenesis is a useful method for introducing mutations to a template plasmid. Of the 10 mutations tried, 7 were successfully obtained. The PCR attempts of I112T and N86D resulted in pWT which could be due the 3'→5' exonuclease proofreading activity of the Tgo polymerase contained in the Expand Long Template PCR System DNA polymerase mix. It is not clear why, despite several attempts, we have been unsuccessful in obtaining I112T. On the other hand, the primers for H48R and N86D contain more than one point mutation. It would be worth considering redesigning the primers for all 3 mutants to increase the efficacy of mutagenesis. The characterization of the mutant proteins is described in the following chapters. Chapter 3 will focus on determining the stability of holo A4S, A4T and G41D and comparing them with pWT. This chapter will also include preliminary data on H80R.

In Chapter 4, the propensity for aggregation of holo A4S and A4T is studied to better understand the mechanism by which these mutants may confer toxicity.

Chapter 3 Stability of ALS-associated hSOD mutants

3.1   Introduction

PCDs are a fast growing subset of modern world diseases, largely due to the complicated nature of the diseases and the lack of known causes. With many PCDs associated with natively folded proteins, mutations associated with the hereditary forms of the diseases tend to destabilize the native state (70). Similarly, studies on purified ALS-associated hSOD mutants have revealed that the mutants are destabilised compared to pWT in the holo state (71-73). The destabilization of the native state can in turn increase the protein's propensity to unfold/misfold or populate aggregation prone intermediates. Mutant hSOD expressed in rabbit reticulocyte lysate have also been shown to be less resistant to proteolysis (74) and hSOD peptide fragments have been found in aggregates from a mutant hSOD mouse model of ALS (49). In this chapter, the thermal stability of the dimer interface mutants A4S, A4T and I113T, in the holo form, will be characterized using differential scanning calorimetry and compared to pWT. In addition, some preliminary DSC data and analysis on G41D and H80R are presented.

3.1.1 Differential scanning calorimetry

The thermal stability of hSOD can be measured using differential scanning calorimetry (DSC) (75). DSC measures the difference in heat capacity between a reference cell, containing only buffer, and a sample cell, containing protein in buffer, as it is heated at a constant rate through its unfolding transition (76). As the protein unfolds, more energy is required to heat the sample cell at the same rate as the reference cell, which produces an endothermic peak in the heat capacity curve (illustrated in Figure 2.1). The area under the unfolding transition peak gives

the calorimetric enthalpy of unfolding (ΔH_{cal}) and reflects the actual change in the enthalpy of

the system. ΔH_{cal} can be expressed by Equation 3.1:

$$\Delta H_{cal} = \int_{T1}^{T2} \Delta C_p \, dT$$

Equation 3.1

where ΔC_p is change in heat capacity upon unfolding and T is temperature.
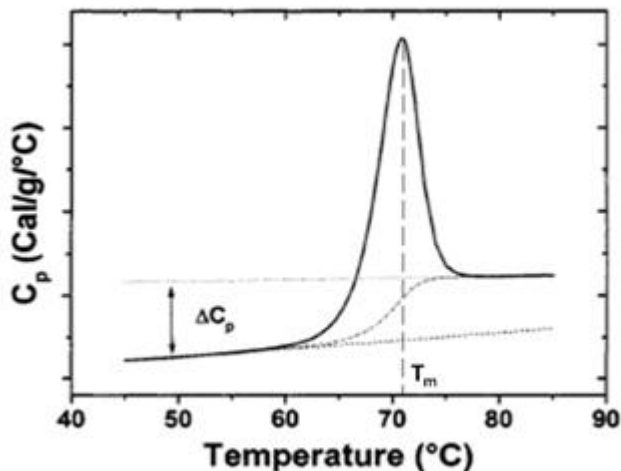
Figure 3.1 The specific heat capacity function of a globular protein. ΔC_p is the difference
between the heat capacity of the native ($C_{p,N}$) and the unfolded ($C_{p,U}$) states which are indicated
by dashed and dotted lines, respectively, and T_m is the temperature where f_u= 0.58 (figure
obtained from (68)).

The van't Hoff enthalpy (ΔH_{vH}) can be obtained by fitting the heat capacity curve to an

appropriate unfolding model. The ratio of ΔH_{vH} to ΔH_{cal} will reflect how well the data fits the

proposed model as well as the size of the cooperative unit of unfolding (76). In the case of

hSOD, unfolding can be fit to a dimer two-state unfolding model,

$N_2 \leftrightarrow 2U$

where the unfolding transition occurs between native dimer (N_2) and unfolded monomers ($2U$)

(28).

For a dimer two-state unfolding model, the unfolding transition is expected to be

asymmetrical and the T_m , the temperature at which half of total dimer is unfolded, is expected to

25

increase with protein concentration (28). A $\Delta H_{vH}/\Delta H_{cal}$ of one indicates that the dimer two-state unfolding model fits the data well. On the other hand, a ratio of greater than one suggests a cooperative unit larger than dimer, *e.g.* the presence of aggregates, while a ratio of less than one indicates a cooperative unit smaller than dimer, *e.g.* the presence of an intermediate (28,75,76). The T_m correlates to the stability of the protein and most fALS-associated hSOD mutations have been found to be less stable than pWT (28,68,77,78). The DSC trace also provides information on the metallation state of the sample as mismetallated protein samples result in traces with multiple peaks or shoulders at lower temperatures. In addition to having lower stability, most fALS-associated hSOD mutants have a $\Delta H_{vH}/\Delta H_{cal}$ larger than unity in the apo form, which indicates an increased propensity to aggregate *in vitro* (68,77,79). It is found that dimer interface mutants A4S, A4T and I113T are destabilized compared to pWT in the holo state. They also have slightly weakened dimer association compared to pWT, consistent with the location of these mutations in the dimer interface. These findings agree with previous data on apo dimer interface mutants, which also had weaker dimer association compared to apo pWT (77,79).

3.2 Methods

3.2.1 Expression of recombinant hSOD

The *E. coli* strain SOD(-/-) (80) was used for large scale protein expression. SOD(-/-) *E. coli* do not produce the two endogenous bacterial SODs, manganese SOD and iron SOD, and are resistant to chloramphenicol and kanamycin (80). Large scale protein expression was performed as described previously (68). Briefly, the recombinant plasmids were transformed into SOD(-/-) *E. coli* (Section 2.2.2) and plated on LB agar containing ampicillin (100 µg/mL), chloramphenicol (30 µg/mL) and kanamycin (30 µg/mL) and incubated overnight at 37 °C. Isolated colonies were grown overnight, at 37 °C, in LB media containing ampicillin (100 µg/mL), chloramphenicol (30 µg/mL) and kanamycin (30 µg/mL). A 1/100 dilution of the overnight cultures was used to inoculate 6 x 1 L 2TY media (16 g bacto-tyrptone, 10 g yeast, 10 g NaCl per 1 L) containing ampicillin (100 µg/mL), chloramphenicol (30 µg/mL) and kanamycin (30 µg/mL). The 2TY cultures were incubated with shaking (200 rpm) at 37 °C until an optical density of 0.6-0.8 at 600 nm was obtained. HSOD expression was then induced by adding isopropyl-beta-D-thiogalactopyranoside (IPTG), $CuSO_4$ and $ZnSO_4$ to final concentrations of 0.25 mM, 0.5 mM and 0.01 mM, respectively. The cultures were incubated with shaking for an additional 8 hours at 37°C, then harvested via centrifugation (4500 x g for 15 min) and the cell pellet was stored at -80 °C until further purification.

3.2.2 Purification of recombinant hSOD

3.2.2.1 Osmotic shock protocol

The osmotic shock (OS) method (81) was used to obtain hSOD from the periplasmic space of the SOD(-/-) cells. Briefly, the cells were resuspended in cold 20 mM Tris-HCl pH 7.5

(25 mL/1 L culture) buffer containing sucrose (20% (w/v) final concentration) and ethylenediaminetetraacetic acid (EDTA; final concentration of 15 mM), incubated in on ice for 20 min with gentle agitation and centrifuged at 4000 x g for 25 min. The cell pellet was then resuspended in cold MilliQ (Millipore Ltd., Bedford, MA) water (20 mL/1 L culture) to release the periplasmic proteins into solution, incubated on ice for 20 min with gentle agitation and centrifuged at 4500 x g for 45 minutes. The supernatant was flash frozen in liquid nitrogen and stored at -80 °C until further purification.

3.2.2.2 Heat treatment and copper charging

The OS supernatant was diluted to a concentration of ~ 0.8 mg/mL in 20 mM Tris-HCl pH 7 buffer and heated to 70 °C with $CuSO_4$ (final concentration of ~1.4 mM) for 25 mins. The $CuSO_4$ is added to ensure proper metallation of hSOD and the high temperature denatures most other periplasmic proteins present in the osmotic shock mixture, which can then be removed via centrifugation at 10 000 x g for 20 min. H80R was heated at 55 °C due to its lower stability.

3.2.2.3 Hydrophobic interaction chromatography

The final purification step was carried out as described previously (68). Briefly, hSOD was eluted from a hydrophobic interaction column using a high to low salt gradient. Fractions containing hSOD were pooled together and dialyzed against MilliQ water with 4 exchanges over 24 hours using 6-8 kDa cutoff dialysis tubing (Spectra/Por® molecularporous membrane tubing; Spectrum Laboratories, Inc., Rancho Dominguez, CA). The dialyzed solution was concentrated using an Amicon ultrafiltration device with a 10 kDa cutoff membrane (YM10 Amicon ultrafiltration regenerated cellulose membrane; Millipore Ltd., Bedford, MA), filtered with a 0.22 μm Acrodisc® syringe filters (Pall Canada Ltd., QC) and stored at -80 °C.

3.2.3 Preparation of apo protein

The apo form (metal free form) of the protein was made using methods described previously (68,73). Briefly, the holo protein was diluted to a concentration of 0.5-1.0 mg/mL and dialysed against EDTA (100 mM EDTA, 50 mM sodium acetate, pH 3.8) and salt (100 mM sodium chloride, 50 mM sodium acetate, pH 3.8) solutions, followed by MilliQ water using a 3.5 kDa cutoff dialysis tubing. Four exchanges over 24 hours were done for each solution/MilliQ water. The dialyzed protein was concentrated using an Amicon ultrafiltration device with a 3 kDa cutoff membrane, filtered with a 0.22 μm Acrodisc® syringe filters and stored at -80 °C.

3.2.4 Protein quantification

3.2.4.1 Lowry assay for protein concentration

A modified version of the Lowry assay (82) was used to determine protein concentrations using bovine serum albumin (BSA) as standards (68). Briefly, 25 μL of BSA standards/samples were incubated with 100 μL of 1 M NaOH for 15 min at room temperature. Then, 1 mL copper solution (2% Na_2CO_3, 0.01% $CuSO_4$, 0.02% sodium tartrate) was added to the standards/samples and incubated at room temperature for 30 min. Finally, 100 μL 50% Folin reagent (Sigma-Aldrich, St. Louis, MO) was added and incubated at room temperature for 30 min at which point, the absorbance of each sample at 750 nm was determined using a Cary 300 Bio UV-Visible Spectrophotometer (Varian Inc., Mississauga, ON).

3.2.4.2 Pyrogallol activity assay for holo hSOD

The pyrogallol activity assay, previously described by Marklund and Marklund (83), was used to determine the specific activity of the holo hSOD mutants (also described in detail in Dr. Jessica Rumfeldt`s thesis (68)). The rate of pyrogallol autooxidation depends on the availability

of superoxide and can be monitored spectrophotometrically (at 420 nm) by a colour change from clear to yellow-brown. The addition of hSOD to pyrogallol will inhibit pyrogallol's autooxidative ability since hSOD competes for superoxide. The specific activity of hSOD will be measured in Units/mg where 1 unit is the amount of hSOD required to reduce the rate of pyrogallol autooxidation by 50%. The average specific activity of holo pWT is approximately 1800 U/mg (73). Many mutants retain full activity; however, a lower than expected specific activity could indicate that the protein is not properly metallated. It may also indicate that a fraction of the protein in the sample is not functional, or the sample as a whole has lower dismutase activity, or a combination all three causes.

3.2.5 Differential scanning calorimetry

Measurements were made using methods previously established in the Meiering laboratory (28,68). Briefly, samples were prepared in 20 mM HEPES pH 7.8 and degassed prior to loading into the calorimeter. All measurements were made using a MicroCal LLC VP-DSC (MicroCal Inc., Northampton, MA) and scanned versus dialysate. Initial DSC scans of holo and apo proteins were done from 15-100 °C and 10-90 °C, respectively, at a rate of 1 °C/min.

The data were then fit to a dimer 2-state unfolding model (Equation 3.2) as well as a monomer 2-state unfolding model (Equation 3.3) as described elsewhere (75,77,79) using the following equations:

$$C_P^{tot}(T) = \frac{\beta \Delta h^2(T)}{RT^2} \frac{f_u(1-f_u)}{2-f_u} + (1-f_u)(A+BT) + f_u(C+DT) \qquad \text{Equation 3.2}$$

$$C_P^{tot}(T) = \frac{\beta \Delta h^2(T) f_u(1-f_u)}{RT^2} + (1-f_u)(A+BT) + f_u(C+DT) \qquad \text{Equation 3.3}$$

where $C_P^{tot}(T)$ is the total specific heat absorption at absolute temperature, T; β is a temperature-independent constant equal to $\Delta H_{vH}/\Delta H_{cal}$ x molecular weight of the dimer; $\Delta h(T)$ is the specific enthalpy of unfolding at T; f_u is the fraction of unfolded protein at T; R is the universal gas constant; A and C are the intercepts and B and D are the slopes of the native and unfolded baselines, respectively. All DSC data fitting was done using Microcal Origin 5.0. The fit provides a fitted T_m (the temperature when f_u = 0.5), a β value and a $\Delta h(T)$ that is the specific enthalpy of unfolding at T_m (in cal/g). The ΔH_{cal} (in cal/mol) can then be obtained by multiplying $\Delta h(T)$ with the molecular mass of the unfolding unit (dimer or monomer) to determine the $\Delta H_{vH}/\Delta H_{cal}$. The DSC scans for holo hSOD were fit to 75% of the endothermic peak due to the presence of an exotherm at high temperatures. The exotherm is probably from irreversible protein aggregation at the high temperatures so that the unfolded baseline is not well defined (77).

For a 2-state unfolding process, T_m should vary with protein concentration as described by the following equation (75):

$$\text{constant} + (n-1)\ln P = -\frac{\Delta H_{vH}}{RT_m} + \text{constant} \qquad \text{Equation 3.4}$$

where P is the total protein concentration of monomers, R is the gas constant and n is the molecularity of the unfolding subunit . Rearranging equation 3.4 indicates that the slope, m, for a $\ln P$ versus $1/T_m$ plot is

$$m = -\frac{\Delta H_{vH}}{R(n-1)} \qquad \text{Equation 3.5}$$

which can then be used to calculate the molecularity of the unfolding subunit.

3.3 Results

3.3.1 Thermal Stability of fALS-associated hSOD mutants

3.3.1.1 Thermal unfolding of holo dimer interface mutants fit a dimer 2-state unfolding model

It has been shown previously that holo hSOD thermal unfolding follows a dimer 2-state model (68,77,79). Figure 3.2 illustrates that holo A4S, A4T and I113T as well as G41D are all fit quite well by the dimer 2-state unfolding model and less well fit by the monomer 2-state unfolding model. This is also indicated by the χ^2 values which are lower for fits to the dimer 2-state model. Dimer 2-state unfolding produces an asymmetrical endothermic peak and has a concentration-dependent T_m. The monomer 2-state fits in Figure 3.2 (B, D, F, H) systematically deviates from the thermograms, where the fits predict a more symmetrical endotherm compared to the data. This is readily apparent around the T_ms and at the beginning of the endothermic peak.

The concentration dependence of the dimer interface mutants is illustrated in Figure 3.3 where the T_m gradually increases with increasing protein concentration. Figure 3.4 are plots of the predicted concentration dependence of T_ms for pWT and the dimer interface mutants calculated from the average fitted parameters to the dimer 2-state unfolding model from Table 3.1. Figure 3.4 shows that the concentration dependence of the experimental T_ms of holo pWT, A4S, A4T and I113T fall within the predicted concentration dependence of their T_ms at the lower protein concentration range. All three mutants have experimental T_ms that deviate from their predicted T_ms at higher protein concentrations. This may be due to their lower stability, leading to an increased propensity to aggregate at higher concentrations. Alternatively, at may be due to increased population of monomer at lower concentrations. Table 3.1 lists the DSC fitted

parameters for holo pWT, A4S, A4T and I113T. Holo pWT's $\Delta H_{vH}/\Delta H_{cal}$ of one indicates that holo pWT fits the dimer 2-state unfolding model well. The ratios for A4S, A4T, A4V and I113T are 0.85±0.07, 0.95±0.13, 0.72±0.18 and 0.89±0.07, respectively, which are quite close to 1. The slightly decreased values could be indicative of the formation of a monomer intermediate, which would be expected since the mutations are near the dimer interface. The $\Delta H_{vH}/\Delta H_{cal}$ for all the mutants also increase with protein concentration, with $\Delta H_{vH}/\Delta H_{cal}$ values closest to unity at higher protein concentrations. This indicates that the dimer is more populated at higher protein concentrations.

From Equation 3.5, the molecularity of the unfolding subunit can be calculated using the following equation:

$$\text{Molecularity} = -\left(\frac{\Delta H_{vH}}{mR}\right) + 1 \qquad \qquad \text{Equation 3.6}$$

where ΔH_{vH} is the average ΔH_{vH} from Table 3.1, R is the gas constant and m is the slope from a $\ln P$ versus $1/T_m$ plot. Table 3.2 list the molecularity for holo pWT and dimer interface mutants as well as dissociation constants, K_d, of the dimer interface mutants in the holo and apo state. The molecularity for pWT is 1.91, which is close to the expected value of 2 for dimer unfolding. On the other hand, the dimer interface mutants all have lower molecularities compared to pWT, consistent with their low $\Delta H_{vH}/\Delta H_{cal}$ in Table 3.1.
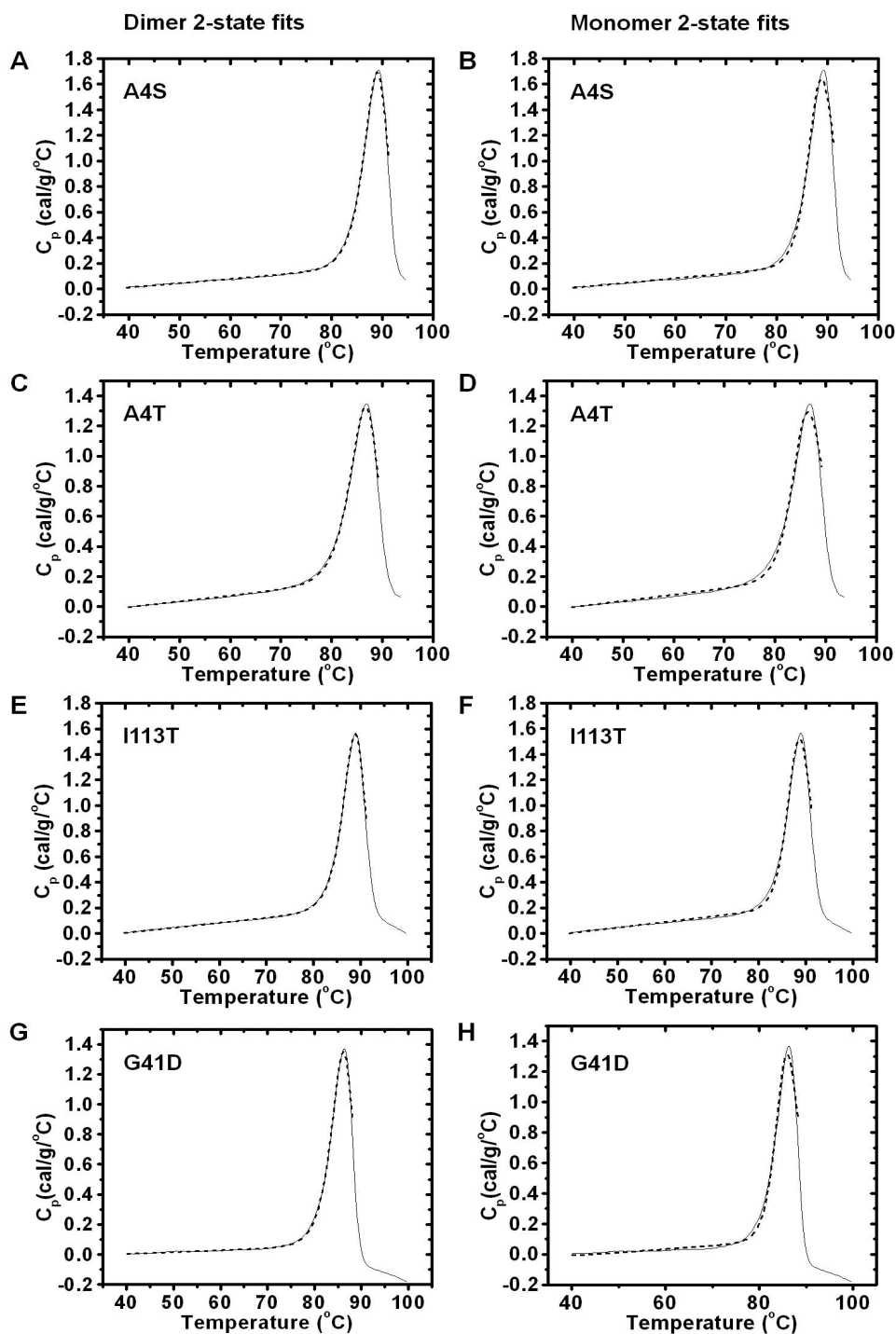
Figure 3.2 Dimer 2-state and monomer 2-state fits of holo dimer interface mutants A4S (A and B), A4T (C and D), I113T (E and F) and G41D (G and F) at protein concentrations of 0.5 mg/mL, 0.39 mg/mL, 0.7 mg/mL and 1.00 mg/mL, respectively. The dimer 2-state fits are on the left while the monomer 2-state fits are on the right. The experimental data and the fits are represented by solid and dashed lines, respectively.
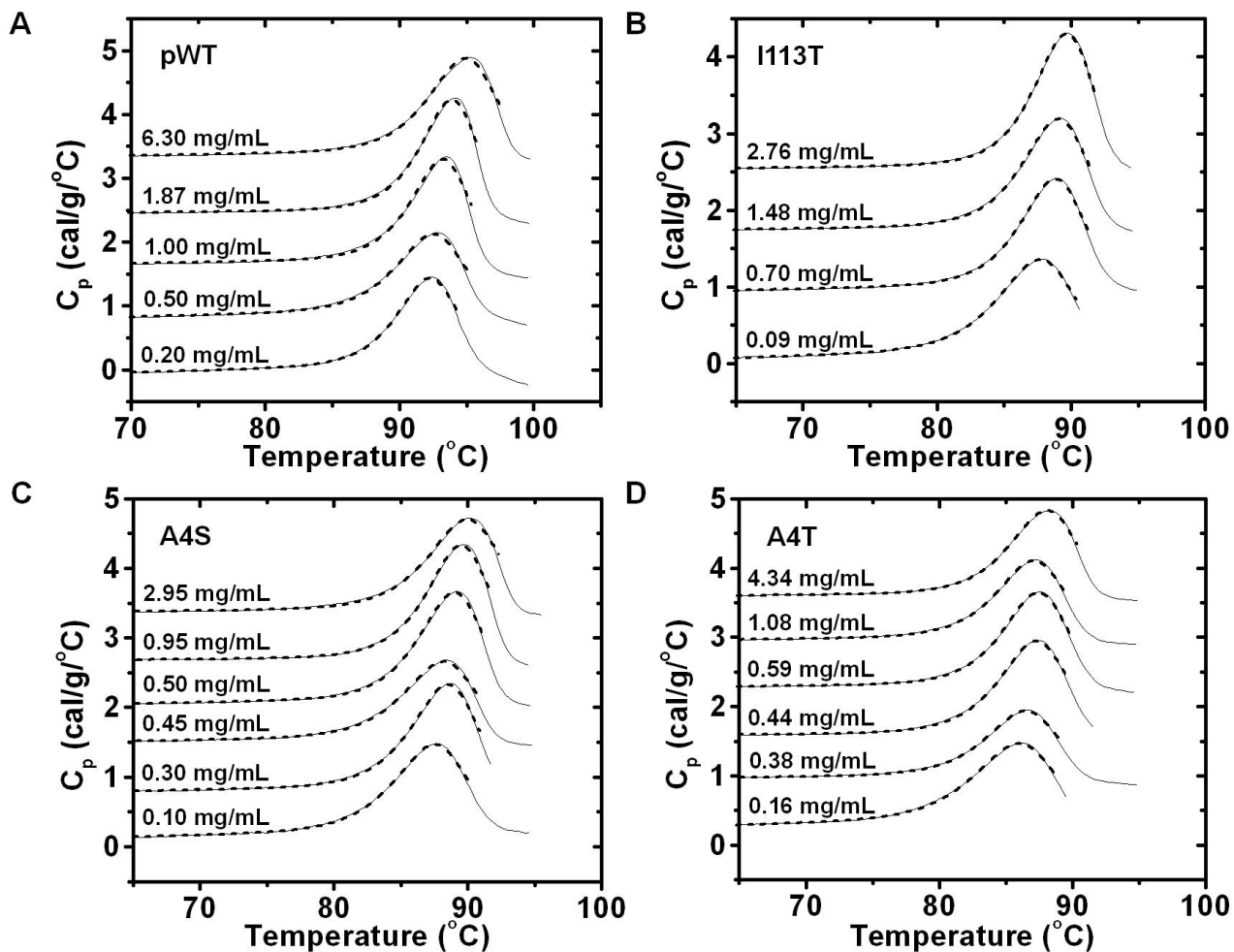
Figure 3.3 Protein concentration dependence of holo pWT and holo dimer interface mutants. DSC thermograms of pWT (A), I113T (B), A4S (C) and A4T (D) at different concentrations are offset for clarity and arranged in increasing protein concentration from bottom to top. The experimental data and the dimer 2-state fits are represented by solid and dashed lines, respectively. The pWT data were obtained by Dr. Jessica Rumfeldt (68).
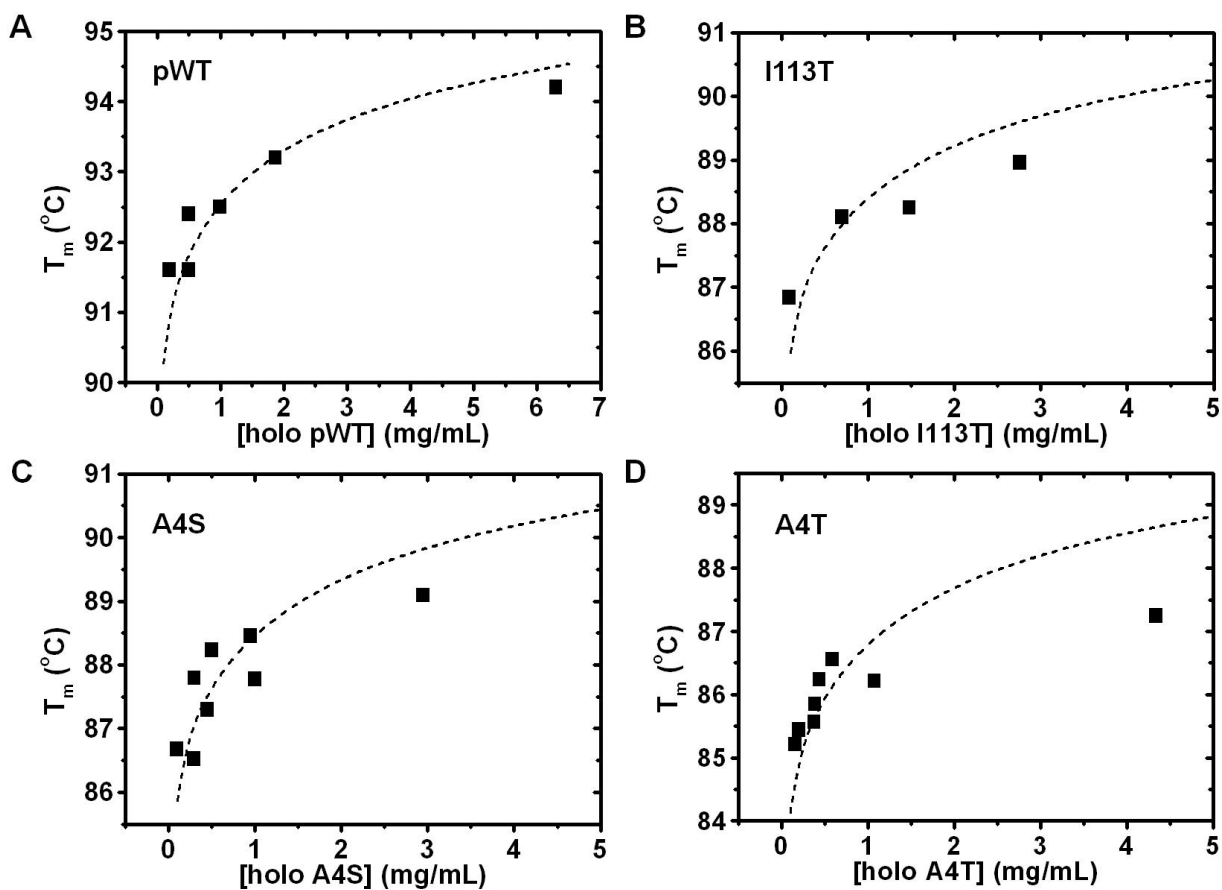
Figure 3.4 Protein concentration dependence of T_m for holo pWT (A), holo I113T (B), holo A4S (C) and holo A4T (D) based on the dimer 2-state model. The squares are the fitted T_m values while the solid lines are the predicted T_m values for each mutant calculated from averaged fitted parameters listed in Table 3.1.

Table 3.1 Fitted dimer 2-state parameters for holo dimer interface mutants A4S, A4T, A4V and I113T and holo pWT.

SOD	[SOD] (mg/mL)	T_m [a] (°C)	ΔH_{vH} [b] (kcal/mol)	ΔH_{cal} [b] (kcal/mol)	$\dfrac{\Delta H_{vH}}{\Delta H_{cal}}$	ΔC_p at T_m [c] (kcal/°C/mol)
pWT*	0.20	91.6±0.2	265.5±15.1	228.8±11.5	1.16	4.12
pWT*	0.50	92.4±0.4	256.5±22.8	231.4±18.3	1.11	4.50
pWT*	0.50	91.6±0.5	230.6±24.3	220.6±20.9	1.05	5.37
pWT*	1.00	92.5±0.5	269.0±30.5	255.0±26.0	1.05	5.80
pWT*	1.87	93.2±0.3	276.9±20.5	270.5±17.8	1.02	7.07
pWT*	6.30	94.2±0.3	238.7±20.2	279.8±20.4	0.85	3.73
Mean±S.D.					1.04±0.10	5.10±1.23
A4S	0.10	86.7±0.0	208.2±3.6	256.1±3.1	0.81	3.85
A4S	0.30	86.5±0.2	184.4±10.1	243.1±11.2	0.76	2.92
A4S	0.30	87.8±0.1	234.2±7.1	276.8±7.0	0.85	3.57
A4S	0.45	87.3±0.0	212.9±3.8	217.0±2.1	0.98	3.95
A4S	0.50	88.2±0.0	238.3±3.0	279.8±2.1	0.85	5.02
A4S[†]	0.95	88.5±0.0	238.2±5.2	261.8±3.1	0.91	*11.21*[d]
A4S[†]	1.00	87.8±0.0	211.1±3.1	253.5±1.7	0.83	4.32
A4S[†]	2.95	89.1±0.0	214.9±2.5	260.1±1.3	0.83	4.60
Mean±S.D.					0.85±0.07	4.03±0.69
A4T	0.16	85.2±0.1	187.9±4.0	254.8±4.2	0.74	1.74
A4T	0.20	85.4±0.1	197.3±6.3	195.5±5.0	1.01	0.04
A4T	0.38	85.6±0.0	209.8±2.2	185.2±1.0	1.13	3.78
A4T	0.39	85.8±0.0	201.5±2.1	251.4±1.3	0.80	3.33
A4T	0.44	86.2±0.1	215.4±7.7	243.6±7.6	0.88	8.13
A4T	0.59	86.6±0.0	230.3±2.0	239.5±0.9	0.96	6.22
A4T[†]	1.08	86.2±0.1	221.5±4.6	207.3±3.4	1.07	4.77
A4T[†]	4.34	87.3±0.0	224.1±1.6	229.9±0.8	0.97	4.34
Mean±S.D.					0.95±0.13	4.04±2.51
A4V[‡]	0.20	86.9±0.0	197.7±1.4	373.9±1.5	0.53	5.88
A4V[‡]	0.50	87.2±0.0	204.2±1.4	333.8±1.0	0.61	6.49
A4V[‡†]	1.00	87.4±0.0	208.4±1.7	232.0±0.8	0.90	3.44
A4V[‡†]	5.00	88.4±0.0	237.5±3.1	279.9±1.5	0.85	4.88
Mean±S.D.					0.72±0.18	5.17±1.33
I113T	0.09	86.8±0.0	200.7±2.0	253.8±1.4	0.79	3.42
I113T[†]	0.70	88.1±0.0	242.0±2.3	248.2±1.6	0.97	4.19
I113T[†]	1.48	88.2±0.0	231.6±2.1	257.1±1.5	0.90	5.51
I113T[†]	2.76	89.0±0.0	260.0±1.6	288.3±0.8	0.90	5.53
Mean±S.D.					0.89±0.07	4.66±1.04
G41D	1.00	85.3±0.4	235.8±5.7	225.2.7±4.4	1.05	6.13

[*] Data obtained and fitted by Dr. Jessica A. O. Rumfeldt (68).

[‡] Data obtained by Dr. Jessica A. O. Rumfeldt (68) and fitted by Helen Stubbs.

[†] Datasets used to calculate free energy plots in Figure 3.5 (B) as well as thermodynamic parameters in Table 3.3.

[a] Errors for ΔC_p of individual fits could not be reliably calculated as they are based on uncertainties from five different variables.

[b] Errors obtained from fitting program.

[c] Errors derived using standard procedures (84) from errors in fitted Δh_{cal} and β obtained from fitting program.

[d] Data point is an outlier and is not included in average ΔC_p.

Table 3.2 Dissociation constants, K_d, and molecularity for pWT and dimer interface mutants. The molecularity was calculated using equation 3.4.

hSOD	K_d apo 37 °C [a] (μM)	K_d holo 65 °C [b] (μM)	Molecularity
pWT	-	-	1.91
A4S	1.6±0.6	-	1.86
A4T	5.1±1.2	-	1.57
A4V	10.0±3.1	48±17	1.39
I113T	3.9±0.1	33±10	1.54

[a] Data from (79).
[b] Data from (77).

3.3.1.2 Holo mutants are destabilized relative to holo pWT

DSC reveals that dimer interface mutants A4S, A4T and I113T as well as G41D are destabilized relative to pWT. This is clearly illustrated in Figure 3.5 (A) where the mutants have lower T_ms compared to pWT and in Table 3.3 where the difference in T_m of the mutants relative to pWT range from -4.7 °C to -7.4 °C. The negative values of $\Delta\Delta G$ (Table 3.3), the change in ΔG of the mutant relative to pWT, and the shift to lower temperatures of the free energy diagrams of the mutants relative to pWT (Figure 3.3 B) also indicate that the mutants are destabilized compared to pWT. Due to errors that may be propagated through long extrapolations of ΔG, the $\Delta\Delta G$ is reported at T_{avg} (88.3 °C - short extrapolation), as well as at physiological temperature (25 °C - long extrapolation).

The change in Gibbs free energy of unfolding, ΔG, for pWT was determined using the average fitted parameters from Table 3.1. On the other hand, ΔG for the dimer interface mutants were determined using only the average fitted parameters of datasets at higher protein concentrations (labelled †) from Table 3.1. This was done as the datasets at higher protein
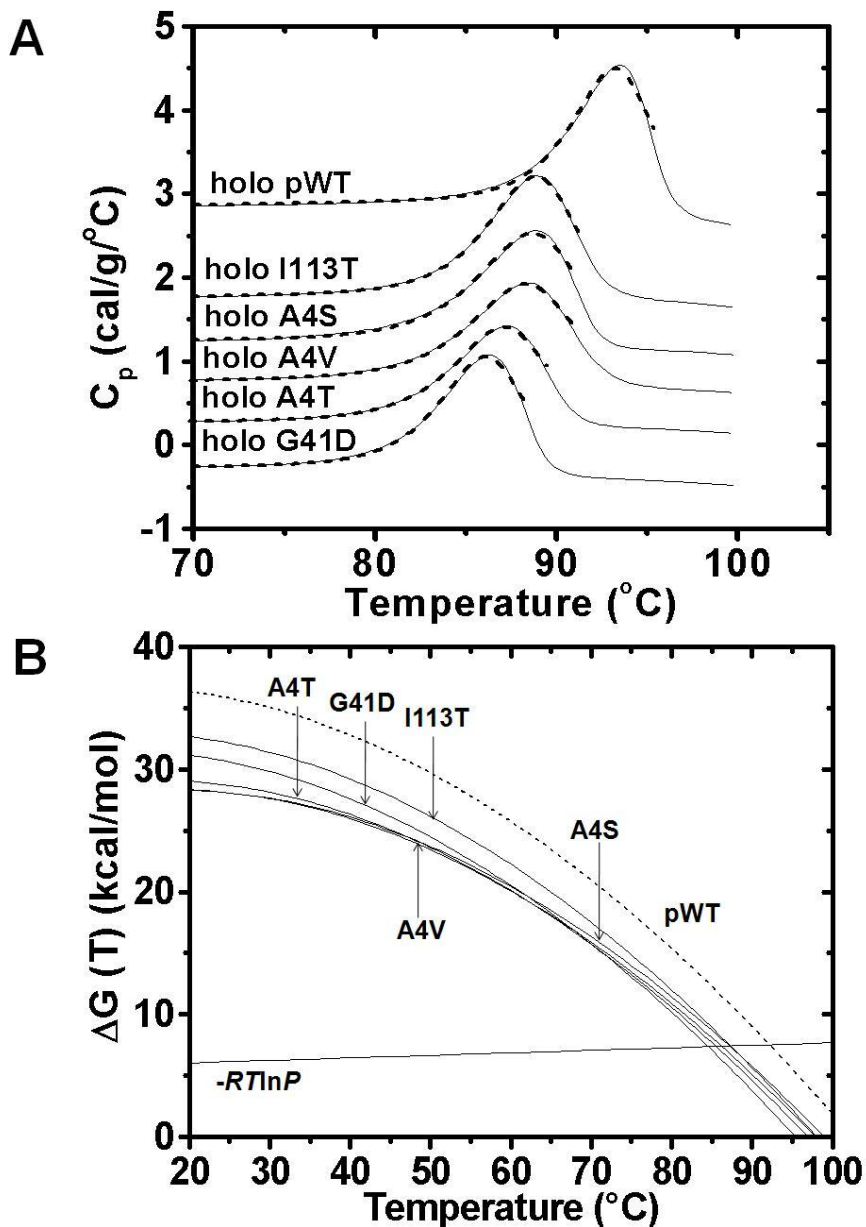
concentrations are more representative of dimer 2-state unfolding and will provide a more relevant comparison with pWT values. A constant ΔC_p of 2.75 kcal/mol (as determined previously for pWT by Dr. Jessica Rumfeldt (68)) instead of the average ΔC_ps from Table 3.1 as the ΔC_ps from the DSC fits are associated with considerable error (85) owing to the lack of a well defined unfolded baseline. The ΔGs at T_{avg} and 25 °C were calculated using the following equations (68,77):

$$\Delta G(T) = \Delta H_{vH}(T) - T\Delta S(T) \hspace{3cm} \text{Equation 3.7}$$

$$\Delta H_{vH}(T) = \Delta H_{vH}(T_m) + \Delta C_p(T - T_m) \hspace{2cm} \text{Equation 3.8}$$

$$\Delta S = \Delta S(T_m) + \Delta C_p ln\left(\frac{T}{T_m}\right) \hspace{2.5cm} \text{Equation 3.9}$$

$$\Delta S(T_m) = \frac{\Delta H(T_m) - \Delta G(T_m)}{T_m} \hspace{2.8cm} \text{Equation 3.10}$$

Figure 3.5 ALS-associated mutants are destabilized relative to pWT in the holo state. (A) DSC thermograms of holo pWT, I113T, A4S, A4V, A4T and G41D at protein concentrations of 1.00 mg/mL, 0.70 mg/mL, 1.00 mg/mL, 1.00 mg/mL, 1.08 mg/mL and 1.00 mg/mL, respectively. The thermograms are arranged from highest to lowest T_m (top to bottom) where the solid lines are experimental data and the dashed lines are the fits to the dimer 2-state unfolding model. The thermograms are also offset for clarity. (B) Free energy diagrams of each mutant relative to pWT in the holo state. pWT is shown as a dashed line while A4T, A4S, A4V, G41D and I113T are shown in solid lines and indicated with arrows. The free energy plots were calculated from average fitted values from higher protein concentration datasets listed in Table 3.1 as they are more representative of dimer 2-state unfolding. The intersection of the "horizontal line", $-RT\ln P$ (for 0.50 mg/ml), with the free energy plots gives predicted t_m for each mutant.

Table 3.3 Thermodynamic parameters of holo fALS-associated mutants A4S, A4T, I113T and G41D compared to pWT. Only datasets at higher protein concentrations (Table 3.1 †) for the dimer interface mutants were used in the calculation for the parameters in this table to avoid any bias that may be contributed from the presence of a monomer intermediate.

Holo isomer	Δt_m [a] (°C)	$\Delta G(T_{avg})$ (kcal/mol)	$\Delta S(T_{avg})$ (kcal/K/mol)	ΔG (25 °C) (kcal/mol)	ΔS (25 °C) (kcal/K/mol)	$\Delta\Delta G\ (T_{avg})$ [b] (kcal/mol)	$\Delta\Delta G$ (25 °C) (kcal/mol)	$\Delta\Delta S$ [c] (kcal/mol)	$\Delta\Delta H$ [d] (kcal/mol)
pWT[*]	-	10.1±0.4	0.66±0.05	35.4±3.2	0.13±0.05	-	-	-	-
A4S	-4.8	6.8±0.3	0.59±0.04	28.1±2.8	0.06±0.04	-3.3	-7.4	-0.06	-26.7
A4T	-6.5	5.7±0.5	0.62±0.01	28.7±1.2	0.09±0.01	-4.4	-6.8	-0.04	-17.9
A4V[‡]	-5.8	6.2±0.4	0.60±0.05	28.1±2.9	0.07±0.05	-3.9	-7.4	-0.05	-23.7
I113T	-4.7	6.8±0.2	0.66±0.04	32.1±2.3	0.13±0.04	-3.3	-3.3	0.00	-3.5
G41D	-7.4	4.9	0.66	30.6±0.5	0.13±0.00	-5.1	-4.9	0.00	-3.6

[a] t_m at 0.5 mg/mL from Figure 3.5 (B).
[b] Change in the ΔG of the mutants relative to pWT ($\Delta\Delta G = \Delta G_{mutant} - \Delta G_{pWT}$).
[c] Change in the ΔS of the mutants relative to pWT ($\Delta\Delta S = \Delta S_{mutant} - \Delta S_{pWT}$).
[d] Change in the ΔH of the mutants relative to pWT ($\Delta\Delta H = \Delta H_{mutant} - \Delta H_{pWT}$).
[*] Data from (68).
[‡] Data from (68) and fit by Helen Stubbs.
T_{avg} = 88.3 °C is the average T_m for pWT and mutants from Table 3.1.
Errors(±) are the standard deviations from multiple datasets listed in Table 3.1. No errors are reported for the single dataset for G41D.

3.3.2 H80R

3.3.2.1 Initial Data

When H80R was initially obtained from the small scale purification, the mass spectrum of its OS contained not only a peak corresponding to H80R but also a fairly large peak corresponding to an approximately +18.5 Da species. Another mass spectrum was obtained after a 16 days incubation period at room temperature. Figure 3.6 illustrates the peak intensities of H80R and the +18.5 Da peak before and after the 16 day incubation. Over time the +18.5 Da species increased as the H80R peak decreased. This indicated that H80R was being modified over time. Figure 3.6 also illustrates that this modification process began either before or during the protein purification process as the pre-incubation sample contained the modification. The addition of 18.5 Da could correspond to the mass of a molecule of water, suggesting that the protein may have been cleaved somewhere between the intramolecular disulfide bonds (C57-C146) of H80R, thus keeping the cleaved protein intact.
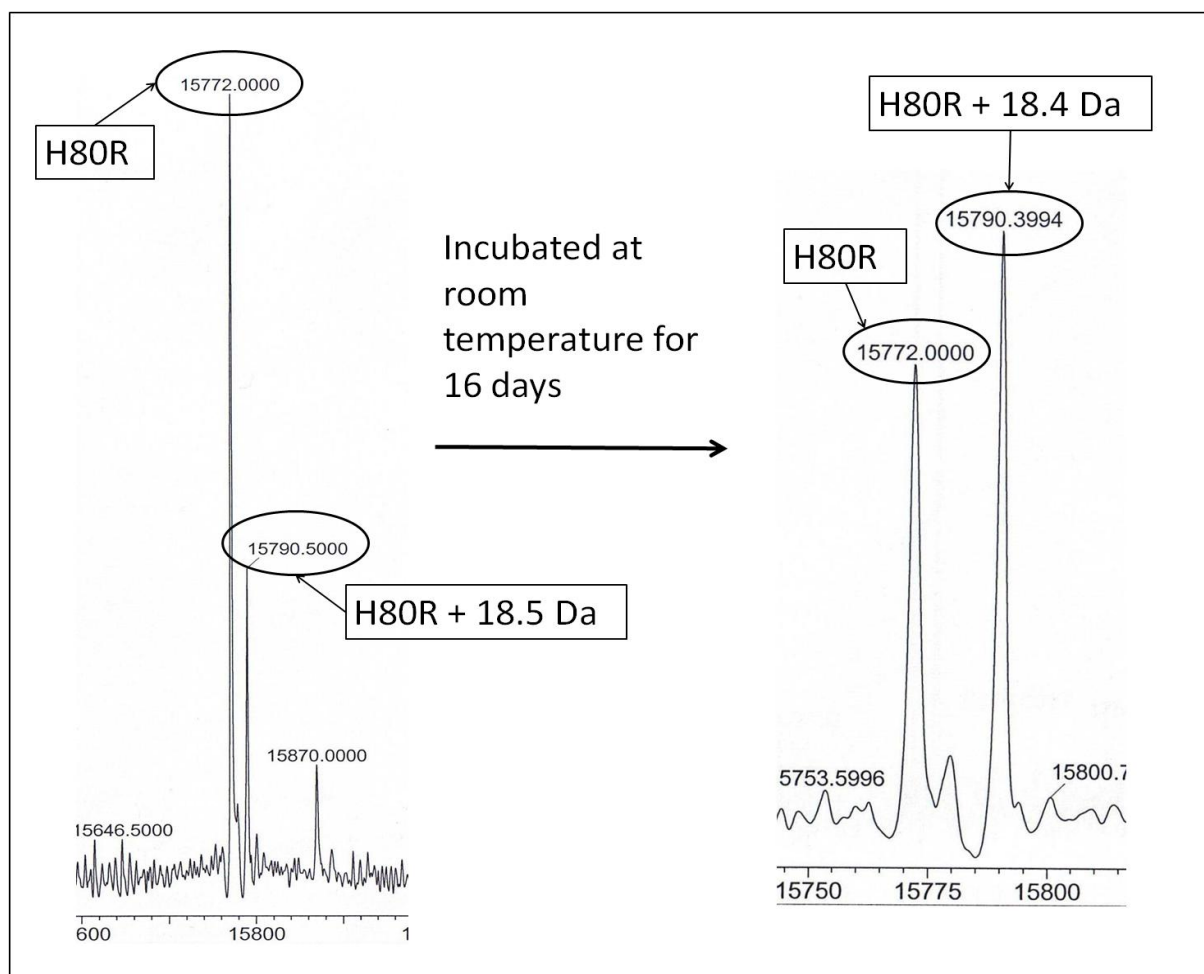
Figure 3.6 Change in H80R species distribution over time. The spectrum indicates conversion of H80R into H80R+18.5 kDa species. The sample is the OS supernatant form a small scale purification of H80R.

3.3.2.2 Identifying the site of cleavage

A time-dependant modification as observed for H80R has never been observed for any other hSOD mutants previously studied in our laboratory. X-ray crystallography data have shown that although H80R does not bind metal in the zinc site, it does contain a metal ion, presumably zinc or copper, in the copper binding site (86). Considering that H80R is a zinc binding site mutant, it may be possible that the active site copper can undergo some kind of aberrant chemistry resulting in the self-cleaving of H80R. Another possible scenario could be

decreased stability of H80R due to the lack of zinc coordination (86), increasing its sensitivity to proteolysis.

To determine where the protein was being cleaved, the OS from a small scale expression was purified using a Nanosep 3K Omega centrifugal device (Pall Canada Ltd., QC) to remove the sucrose as well as any small fragments that may be in the sample. The OS and the slightly purified sample were incubated for 17 hours at 37 °C and at room temperature. Figure 3.7 is an SDS-PAGE of H80R incubated at the different temperatures. The unreduced samples (Figure 3.7 Lanes 9-14) contain 2(3) major bands of ~15 kDa in size. We suspect that the larger band(s) corresponds to the cleaved species as it would have a more expanded structure and travel slower through the gel. The same samples reduced with 10% β-mercapthoethanol (βme) (Figure 3.7 Lanes 3-7) reveal that one of the larger bands has been replaced by 2 smaller fragments of ~8.1 kDa in size.

The specific masses of the fragments were determined using mass spectrometry. sample was fully reduced. Figure 3.8 shows the reduced (B) and non-reduced (A) mass spectra of the slightly purified H80R that had been incubated for 17 h at 37 °C. To ensure that the entire sample in Figure 3.8 (B) was reduced, the sample was incubated overnight under reducing conditions in 1% βme. Figure 3.8 (A) is the spectrum for the non-reduced sample and contains peaks for disulfide intact H80R (15772 Da) and disulfide intact H80R+18.5 Da (15790.5 Da) while Figure 3.8 (B) is the spectrum for the reduced sample and contains reduced H80R (15774.5 Da), no H80R+18.5 Da peak and peaks at 7211 Da and 8580 Da. Using the MassLynx program, it was determined that the 7211 Da fragment corresponds to residues 1-69 while the 8580 Da fragment corresponds to residues 70-153. Therefore, H80R was being cleaved between

residue R69 and K70. Both spectra in Figure 3.8 contain a ~H80R+98 Da species. This +98 Da

peak is present in most of our protein preparations as is thought to correspond to a sulphate

adduct (artefact from our protein expression and purification protocol).
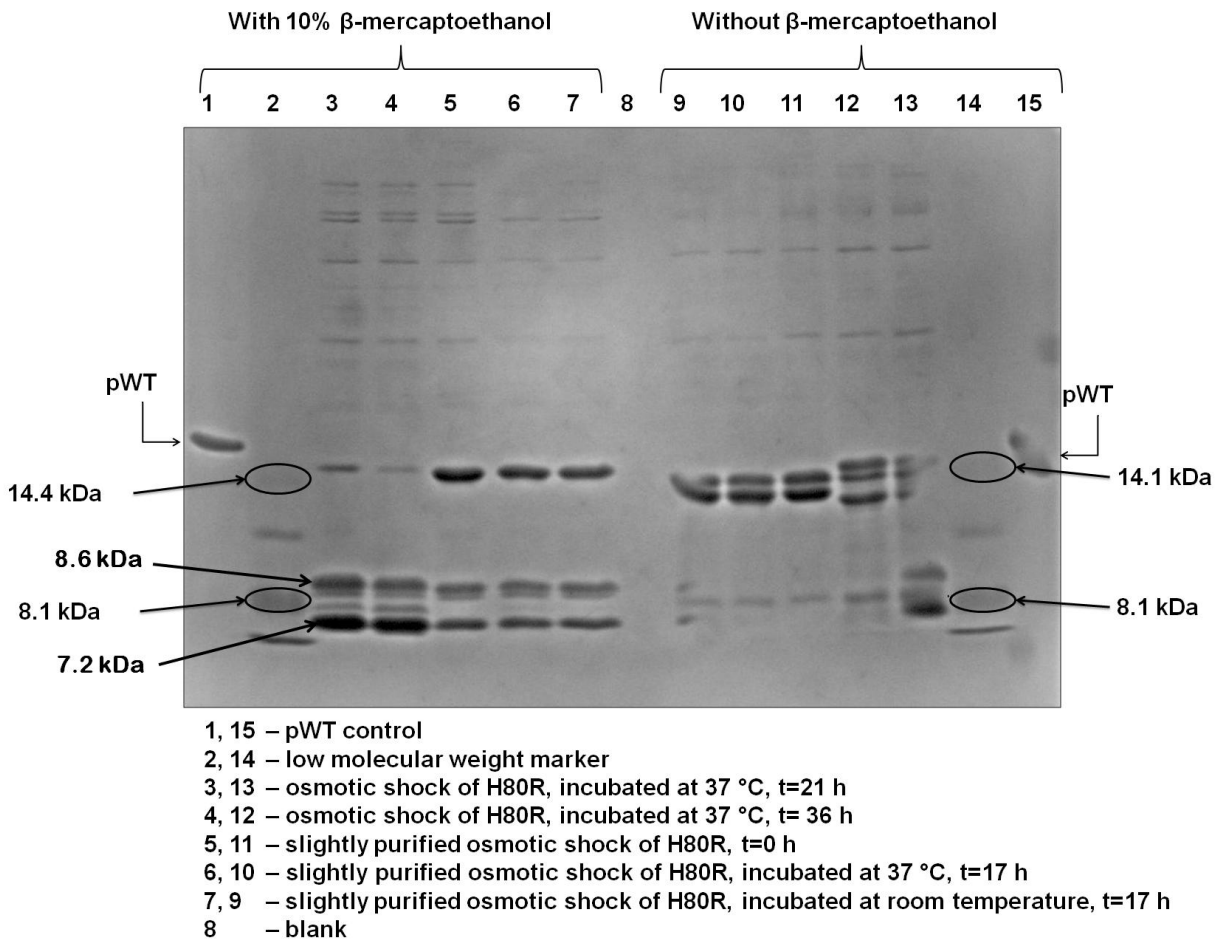
**Figure 3.7 SDS-PAGE of H80R OS incubated under different conditions.**
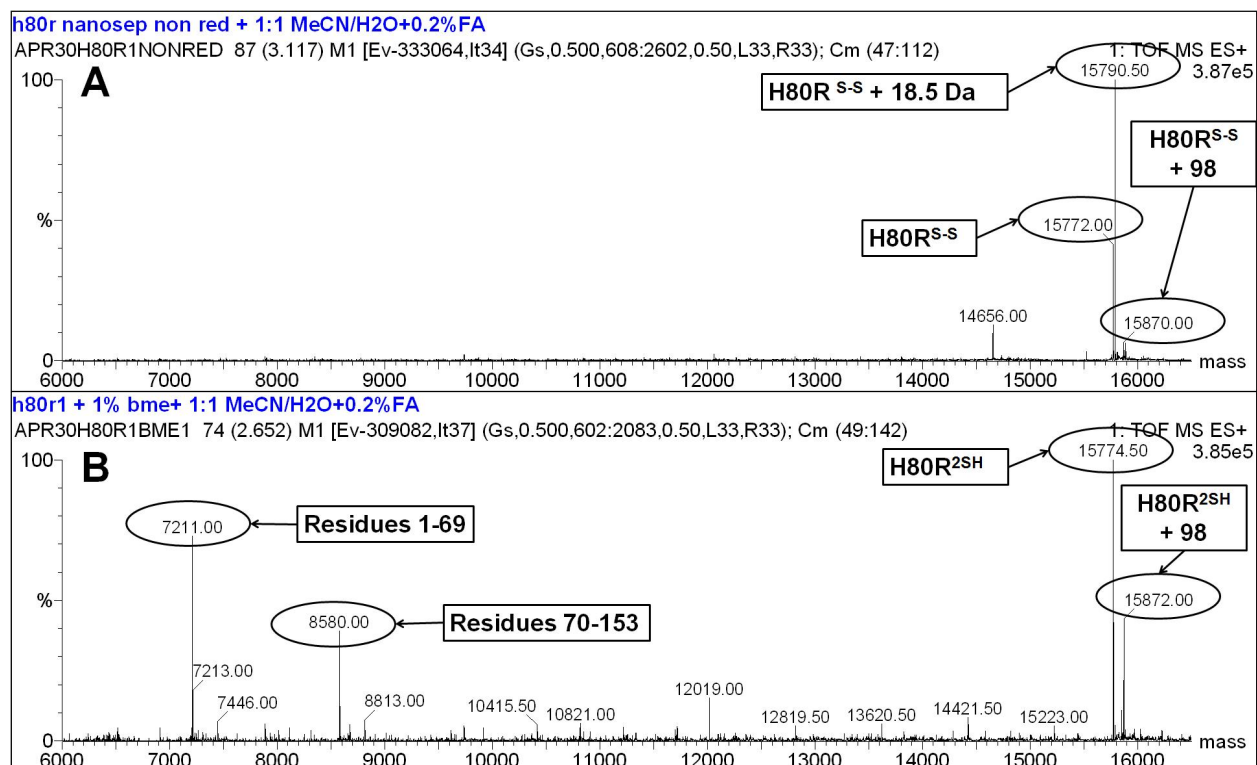
Figure 3.8 Mass spectrum of fragmented H80R in non-reducing (A) and reducing (B) conditions. The H80R sample was incubated at 37 °C for 17 hours before the mass spectrum was obtained, at which point, an aliquot of the sample was reduced with 1% βme. Both aliquots were sprayed in a solution of 1:1 acetonitrile:water mixture with 0.2% formic acid.

3.3.2.3 Purification of H80R

Due to the fact that H80R is a zinc binding mutant, our initial assumption was that copper was undergoing non-native chemistry in the active site, resulting in the cleavage of the protein. Accordingly, to determine the optimal expression conditions, H80R cultures were grown in three conditions: without metals, with both copper and zinc and with only zinc. The protein was then prepared from *E. coli* via the regular osmotic shock protocol (Section 3.2.2.1). The three sets of OS were then heat treated at 50 °C, 60 °C and 70 °C with and without the addition of copper. This was done to determine the optimal temperature for heat treatment which should not only increase the purity of the OS samples but also minimize loss of H80R. Figure 3.9 shows an SDS-

PAGE illustrating the results for the different H80R expression and heat treatment conditions. H80R grown with zinc had the highest yield compared to the cultures grown with both copper and zinc or without metals, suggesting that the addition of zinc helps stabilize H80R. Figure 3.9 also indicates that heat treatment without the addition of copper does not significantly increase the purity of the OS. Samples heat treated with copper at 70 °C (Figure 3.9 Lanes 6, 13 and 19) have a decreased amount of H80R compared to the samples heat treated at lower temperatures, indicating that H80R likely aggregates at 70 °C in the presence of copper. Interestingly, reduced samples from all three sets of OS that were heat treated with copper (Figure 3.9 Lanes 21-23) contain a smaller fragment that does not show up in their unreduced counterparts (Figure 3.9 Lanes 4, 11 and 17), further implicating copper's role in the cleavage of H80R. In light of these results, H80R preparations were expressed with zinc, for higher yield, and , initially, not heat treated prior to purification on the hydrophobic interaction column as heat treatment without copper did not increase the purity of the OS. The apo H80R was made from purified as isolated preparations that were heat treated with copper at 55 °C. This was due to the low yields from the non-heated treated samples attributed to protease activity during the protein purification process as well as the non-ideal elution profile of non-heat treated H80R on the hydrophobic interaction column. All the as isolated H80R preparations were checked using SDS-PAGE with βme after purification and contained only whole H80R.
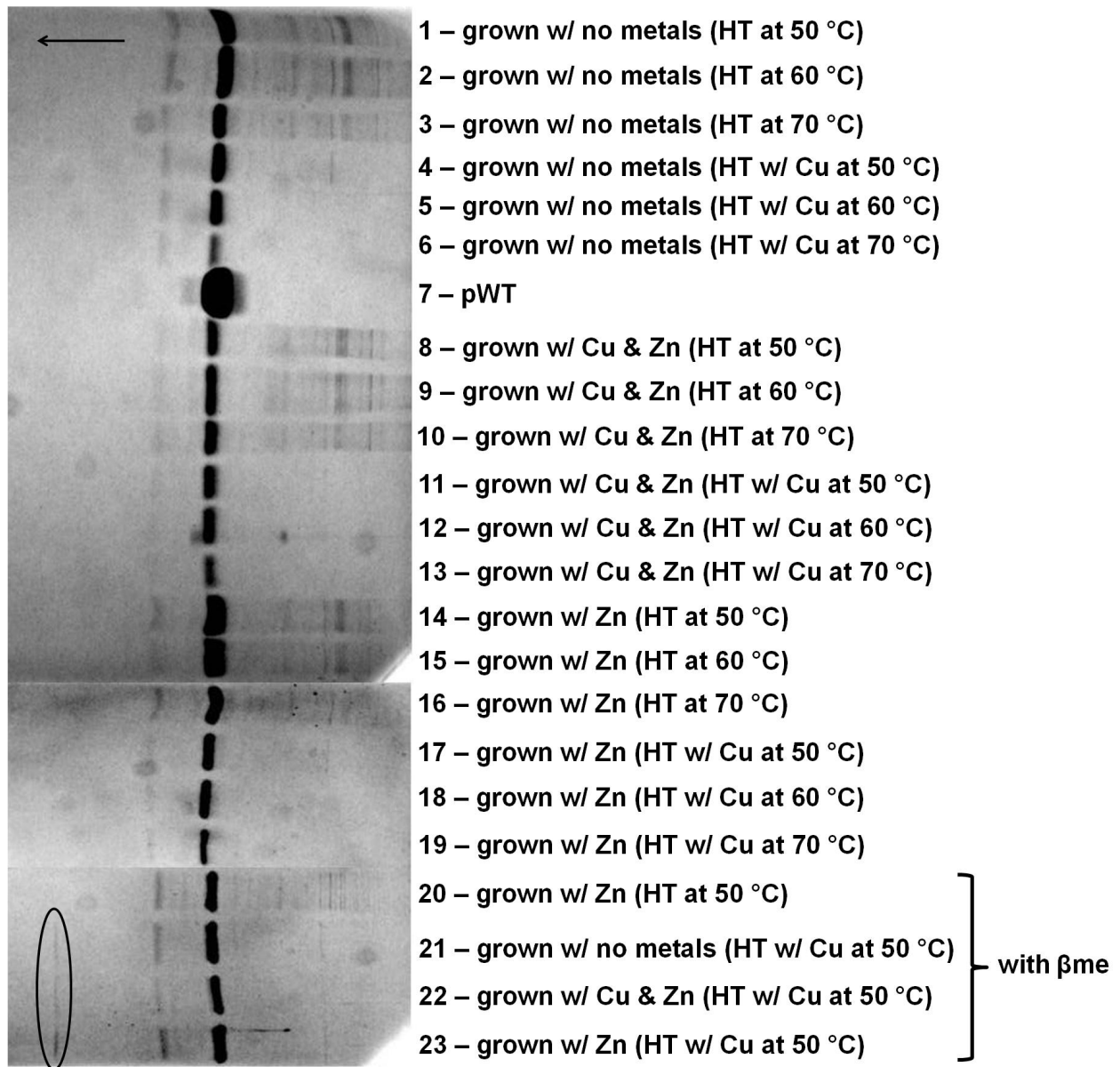
Figure 3.9 SDS-PAGE of H80R grown and heat treated with different conditions to determine the most optimal set of expression parameters. H80R was grown without metals (1-6), with both copper and zinc (8-13) and with only zinc (14-19). The osmotic shock solutions from these were then heat treated with or without copper at 50 °C, 60 °C and 70 °C. Samples in lanes 20-23 were run with 10% βme. Lanes 21-23 appear to have a low molecular weight fragment that is not present in lane 20, or any other lanes.

3.3.2.4 Preliminary results on H80R stability

The thermal stabilities for the purified as isolated form and the apo form of H80R were determined using DSC. Figure 3.10 shows thermograms from two different preparations of as isolated H80R as well as apo preparations of H80R. The as isolated thermograms contain a large endothermic peak with a T_m of ~60 °C while the endothermic peak of the apo samples has a T_m of ~59 °C. However, all the thermograms, with the exception of (d), contain a shoulder with a T_m of ~74 °C. When the samples were rechecked using SDS-PAGE with βme, the samples contained a small amount of fragments similar to those observed in Figure 3.7. This suggested that the fragmentation process was either occurring while the samples were stored at -80 °C or that it was a fast process occurring within the time required to prepare the samples. The shoulder at 74 °C is perhaps due to the unfolding of aggregates of the fragmented H80R. Despite the presence the fragmented species of H80R, the T_m of apo H80R at 59 °C indicates that it has comparable thermal stability to apo pWT, which has a T_m of ~59.1 °C (77). The lack of protein concentration dependence of apo H80R over a concentration range 0.76-1.43 mg/mL suggests that apo H80R may be unfolding via a monomer 2-state unfolding model.
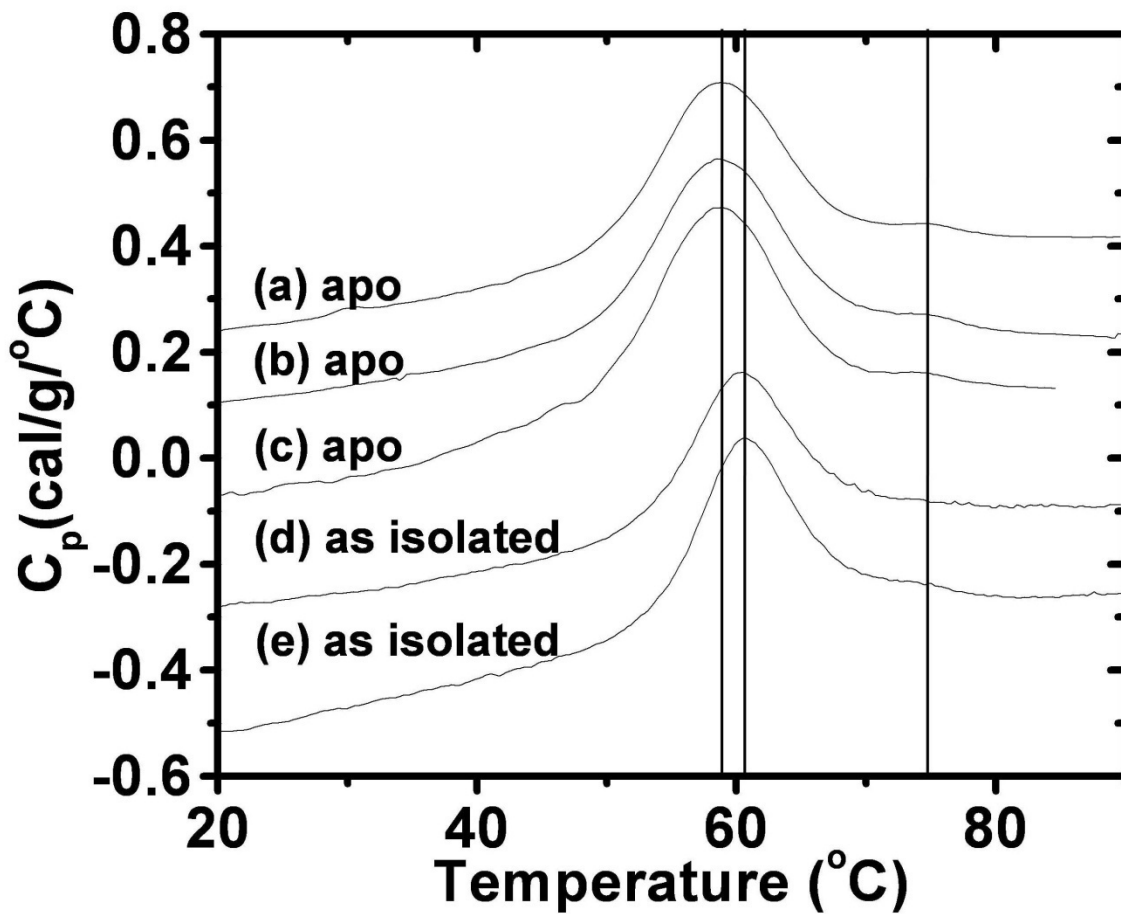
Figure 3.10 DSC thermograms of as isolated (d and e) and apo (a-c) H80R. The three apo samples, a, b, and c, were at protein concentrations of 1.43 mg/mL, 0.97 mg/mL and 0.76 mg/mL, respectively, while the as isolated samples, d and e, were at protein concentrations of 0.46 mg/mL and 0.43 mg/mL.

3.4 Discussion

3.4.1 Dimer interface mutants and G41D are destabilized compared to pWT in the holo state

The thermal stabilities of the mutants relative to pWT in the holo state were determined using DSC. The mutants have comparable specific activities, with the exception of G41D, to pWT which has a specific activity of 1800±200 U/mg (77). The dimer interface mutants A4S, A4T and I113T have average specific activities of 1943±63 U/mg, 1736±260 U/mg and 1668 U/mg, respectively, while G41D has a specific activity of 1538 U/mg (± S.D. of different batches of protein). However, the thermogram for G41D does not appear to contain multiple peaks or shoulders, suggesting that the sample is homogeneous. Alanine 4 is located in β-strand I, at the edge of the dimer interface, and has its side chain pointing into the β barrel. On the other hand, isoleucine 113 is located in loop 6 and points into the dimer interface. The high specific activities of the dimer interface mutants are not unusual as they are located, structurally, quite far away from the metal binding region. It has also been found that most non-metal binding region mutations do not affect the activity of hSOD (19). The lower activity of G41D may be due to its close proximity to the MBR. Glycine 41 is located at the beginning of β-strand IV, which then extends to the zinc binding loop. The introduction of a charged residue at the edge of the β barrel could also perturb the integrity of the β barrel, which in turn would affect the structure of the active site. Interestingly, recent computational studies indicated that mutations located away from the dimer interface or MBR affect the integrity of both the dimer interface and MBR(36).

All the mutants are destabilised relative to pWT in the holo form as reflected by their lower T_ms and ΔGs. This is consistent with previous data obtained on holo hSOD mutants where

mutants were shown to be destabilized via thermal unfolding (28,71)((72) Chapter 4) ((73) Chapter 2) as well as chemical denaturation (78)((68) Chapter 2). The lower ΔG values for the dimer interface mutants are due to lower ΔH_{vH} which are compensated by their lower ΔS values. Previously studied mutants (A4V, G85R, G93A/D/R/S/V and E100G) are also enthalpically destabilized in the holo state (68,77). Interestingly, G41D and I113T have $\Delta\Delta S$ values of 0 and only a small decreases in ΔH_{vH} relative to pWT. Unlike the other mutants studied here, G41D is not a dimer interface mutant. It is located at the beginning of β-strand IV and also replaces a non-polar residue with a charged residue. In fact, G41D is one of the few mutations in hSOD that increases the net negative charge of the protein as the majority of ALS-associated mutations decrease the net charge of hSOD (87). It is worth noting that the dimer interface mutants are associated with short disease durations while G41D has relatively long duration (Table 2.1) despite the fact that G41D has the lowest T_m and has comparable $\Delta\Delta G$ at physiological temperature relative to the dimer interface mutants. The long duration of G41D could be attributed to the increase in net charge of the protein which is predicted to decrease aggregation by increasing electrostatic repulsion the protein molecules (88).

3.4.2 Dimer interface mutants have decreased dimer stability

Although the dimer interface mutants are well fit to the dimer 2-state model, their low $\Delta H_{vH}/\Delta H_{cal}$ ratios are indicative of some formation of a monomer intermediate. Due to mass action, the monomer intermediate would be more populated at low protein concentrations while the dimer would be more populated at high protein concentrations (79). This change in molecularity is exhibited by an increase in $\Delta H_{vH}/\Delta H_{cal}$ ratio towards unity with increasing protein concentration and can be observed for the dimer interface mutants (Table 3.1), where the

lower $\Delta H_{vH}/\Delta H_{cal}$ ratios tend to correlate with lower protein concentrations. This trend is found in all the holo dimer interface mutations studied in our laboratory which includes A4S, A4T, A4V (68) and I113T as well as non-dimer interface mutants including E100G (68), G93A and G93R (77). However, monomer 2-state fits for the dimer interface mutants and G41D show systematic deviations from the DSC thermogram similar to those observed for pWT (28), indicating that these mutants do not unfold in a purely monomer 2- state manner. It in worth noting that apo A4V and H46R have been shown to thermally unfold in a 3-state monomer intermediate unfolding mechanism (79). In addition, chemical denaturation studies on holo pWT, G85R, E100G and G93A and apo G85R, G93R, E100G and I113T reveal that they undergo a 3-state monomer intermediate guanidinium chloride-induced denaturation (68,72,78).

Additionally, isothermal titration calorimetry (ITC) on holo A4V and I113T at 65 °C indicated that these mutants had weaker dimer association compared pWT. ITC of holo A4V and I113T gave dissociation constants (K_d) of 31 μM and 25μM, respectively, while holo pWT did not give significant heats of dissociation (quantifiable dissociation heats for the only first ~2 injections), and therefore, a K_d could not be determined (77). Similarly, the G93A/D/R mutants did not give significant heats of dissociation. However, the G93 mutants had more injections with quantifiable heats of dissociation compared to pWT, indicating that they have a weaker dimer interface compared to pWT (77). ITC experiments conducted on apo hSOD at 37 °C also provide evidence for weaker dimer association in ALS-associated mutants (79). Similar to holo pWT, apo pWT did not give significant heats of dissociation at 37 °C while dimer interface mutants A4S, A4T, A4V and I113T gave K_ds of 1.6 μM, 5.1 μM, 10.0 μM and 3.9 μM, respectively (79). On the other hand, non-dimer interface mutants H46R and G93S gave K_ds of

0.5 µM and 1.2 µM, respectively (79). It is not surprising that apo A4V had the highest K_d out of all the mutants as DSC indicated that A4V unfolds via a monomer intermediate. This is because the dimer interface is sufficiently destabilized compared to monomer stability, enabling the detection of the two processes in DSC. On the other hand, apo H46R which also unfolds with a monomer intermediate had the highest measurable K_d. This is because apo H46R has very high monomer stability coupled with a dimer interface that is only mildly destabilized compared to pWT (79), which also enables the detection of the two processes in DSC. Accordingly, the monomer intermediate is never significantly populated if a mutant has a strong dimer interface or a destabilized monomer. In light these results, it would be sensible to investigate if holo A4S, A4T and I113T undergo a 3-state monomer intermediate unfolding mechanism.

3.4.3 H80R

The presence of fragments in all the preparations of H80R regardless of the purification conditions is perplexing and the reason for this has yet to be resolved. It is possible that aberrant copper chemistry is responsible for the fragmentation of H80R. The formation of fragments after storage in -80 °C suggests a metal catalyzed process. Mutant hSODs have been shown to participate in non-native chemistry *in vitro* (40,53) and although copper was not added to the initial as isolated preparations of H80R, the samples may contain small amounts of copper from the growth media. Figure 3.11 illustrates the close proximity of residues R69 and K70, the cleavage site, to the active site of hSOD as well as H80R, the mutation site. On the other hand, a study conducted by Bruns *et al.* indicated that H80R has decreased resistance to proteolysis (74). The cleave site is located in the zinc binding loop which, in the absence of zinc coordination, has been shown to be disordered (86). An unstructured zinc loop in the mutant may have an enhanced susceptibility to proteolysis.
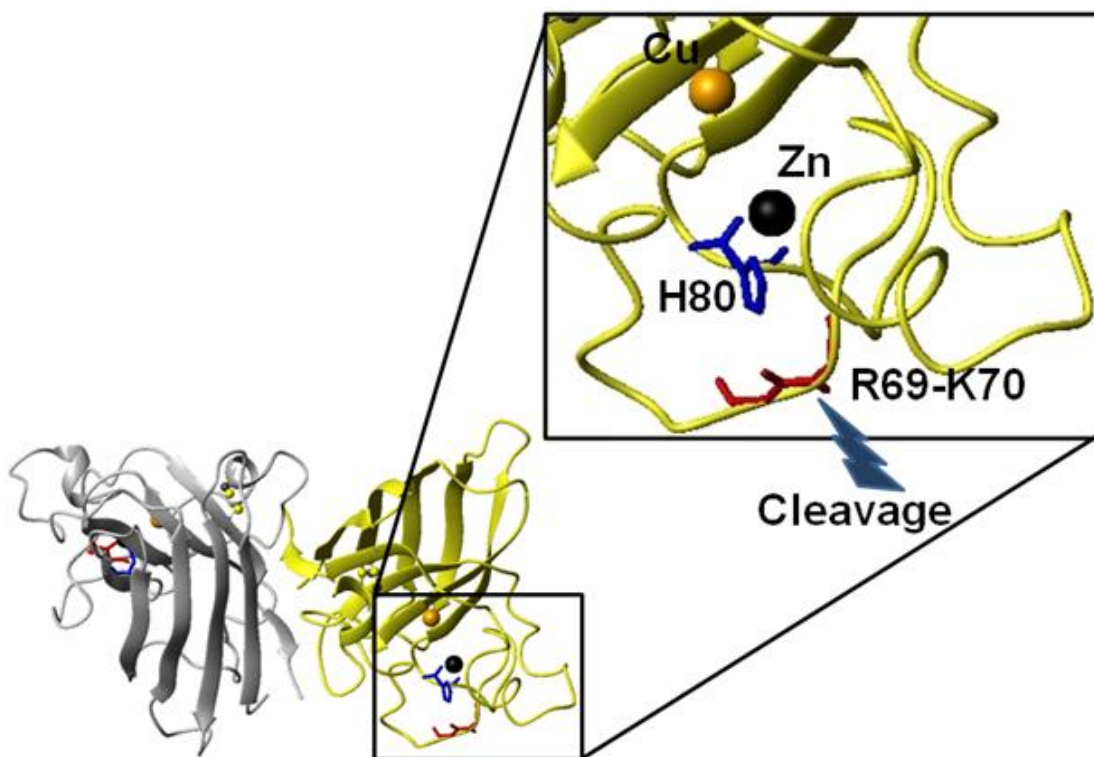
Figure 3.11 Site of cleavage in H80R. Prepared using MolMol (29) and PDB coordinates 1SOS (30). Each monomer contains a Zn^{2+} and a Cu^{2+} ion depicted as black and orange spheres, respectively. Inset is a magnification of the metal binding sites as well as the R69-K70 site where cleavage occurs.

3.4.3 Correlations with disease

Since the discovery of a genetic link between hSOD and ALS (21), many studies have been focussed on finding the common denominator of hSOD toxicity. Due to the high stability of the holo hSOD, including the mutants (89), many studies have suggested that the toxic form of hSOD is the more destabilized apo form (90) or the disulfide reduced apo form which is proposed to be the most immature form of hSOD in the cell (91). However, it has been found that destabilization of the apo protein is not a common feature for all fALS-associated mutants (92). A recent article by Wang *et al.* revealed a correlation between disease durations and the sum of aggregation propensity and instability of the mutants (64). The correlation, although

compelling, only analyzes 28 different mutants due to the limited amount of data available. Considering the complicated nature of ALS, it is likely that there is no common denominator and that the different mutants associated with ALS confer toxicity via different mechanisms, all of which may lead to increased population of some sort of destabilized species that has increased propensity to aggregate compared to holo WT.

Chapter 4 *In vitro* aggregation of holo pWT and dimer interace mutants

4.1   Introduction

As in many other neurodegenerative diseases, protein aggregation is a hallmark of ALS pathogenesis (2). *In vitro* studies have shown that fALS-associated hSOD mutants have an increased propensity to aggregate (73,93) while x-ray diffraction and nuclear magnetic resonance studies have shown that the partially metallated, as well as fully metallated, S134N hSOD mutant tend to generate protein oligomers (94,95). More importantly, aggregates from neuronal cell line (13) and mice model studies of fALS (39,96,97) as well as fALS and some sALS patients have been found to contain hSOD (14,50,51). It is not known if the hSOD found in these aggregates retains their metal ions; however, given that the major species of hSOD in the cell is in the holo form (77), it is plausible that aggregation could occur from holo hSOD.

Various studies on hSOD aggregation have focused on either the apo (90) or mismetallated forms of hSOD, or on the reduced form (91), considering holo hSOD too stable to give rise to aggregates in ALS (89). A recent study by Banci *et al.* demonstrated that disulfide intact apo wildtype hSOD formed aggregates at close to physiological conditions of pH 7, 37 °C and a protein concentration of 100 μM, while both holo wildtype hSOD and holo pWT did not (90). The data from this study contradicts the results previously obtained by the Meiering lab where holo pWT as well as holo forms of fALS-associated mutants have been shown to form aggregates when incubated without agitation at physiologically relevant conditions of pH 7.8 and 37 °C (77) (Y. M. Hwang unpublished data). This chapter investigates the aggregation properties of holo dimer interface mutants A4S and A4T and possible correlations to thermal stability and

disease duration. The aggregation profiles indicate that the mutants have increased aggregation propensities and also provide information regarding the possible aggregation mechanisms. In this chapter, dynamic light scattering is used to monitor aggregation of dimer interface mutants A4S and A4T as well as pWT in the holo state.

4.1.2 Dynamic light scattering

Dynamic light scattering (DLS) is one of the tools commonly used to monitor protein aggregation (98,99). DLS utilizes the principles of Brownian motion to measure the size of particles in a sample solution. A detector located at a fixed angle and distance with respect to an incident light beam, picks up light scattered by particles in the sample solution, which is located between the detector and the light source. The intensity of scattered light fluctuates about an average intensity and the time dependence of these fluctuations are related to the diffusion coefficient, D, of the particles in solution (90Plus Particle Sizer Instruction Manual). The diffusion coefficient reflects the speed of particle movement and is inversely related to particle size as described in the Stokes-Einstein equation:

$$D = \frac{k_B\, T}{3\pi\, \eta\, d} \hspace{4cm} \text{Equation 4.1}$$

where k_B is the Boltzmann constant, T is the absolute temperature, η is the viscosity of the sample solution and d is the diameter of the particle, which is assumed to be spherical.

The light scattering measurement is then divided into small time intervals or delay times, τ, which are much shorter than the time required for the fluctuation to return back to the average scattered intensity. The autocorrelation function, $C(\tau)$, is a plot of the signal intensity within τ as a function of time between τ. With increasing delay times, the correlation between the

58

intensity products within τ decreases and is eventually lost. The autocorrelation function is an exponential function expressed as

$$C(\tau) = A\, e^{-\Gamma\tau} + B \qquad\qquad \text{Equation 4.2}$$

where A is an instrument dependent optical constant, B is the autocorrelation baseline, τ is the delay time and Γ is the decay rate constant expressed by

$$\Gamma = Dq^2 \qquad\qquad \text{Equation 4.3}$$

where D is the diffusion coefficient of the particle in solution and q is the magnitude of the scattering vector, which depends on the instrument and sample expressed by

$$q = \frac{4\pi n}{\lambda_o}\, sin\left(\frac{\theta}{2}\right) \qquad\qquad \text{Equation 4.4}$$

where n is the refraction index of the sample solution, λ_o is the wavelength of the incident light beam and θ is the scattering angle. Because larger particles in a sample move slower through the sample solution, they have smaller diffusion coefficients, which results in a slower decay. Figure 4.1 shows the autocorrelation function for a larger and a smaller particle.
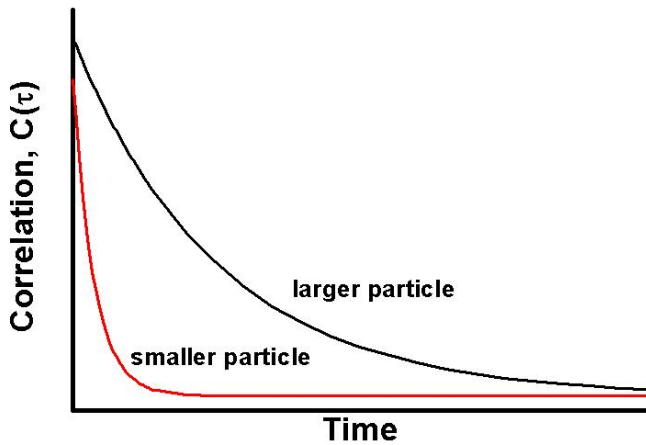
Figure 4.1 Autocorrelation functions of a large and small particle.

Dynamic light scattering can be used to monitor particle size changes over time and has been successfully used to monitor protein aggregation *in vitro* (77,100). In the case of samples with more than one particle size distribution, the autocorrelation function will contain exponentials from each particle size distribution. Algorithms such as cumulants (101) and CONTIN (102) deconvolute the different exponentials and provide the hydrodynamic diameter of the particles in solution.

4.1.2 Nucleation-dependent protein aggregation

Many disease-associated proteins have been shown to aggregate through a nucleation-dependent process involving three phases: lag, growth and plateau (10,103). This process is associated with a sigmoidal aggregation profile (Figure 4.2) and a lag phase that is associated with the formation of thermodynamically unfavourable nucleus (104,105). Nucleation-dependent protein aggregation typically is also characterized by a protein concentration dependence of the lag phase whereby the lag phase shortens with an increase in protein concentration (104). Another feature of nucleation-dependant protein aggregation is a seeding-effect, whereby the addition of preformed aggregates eliminates the lag phase or nucleation step required for aggregate formation (10,103). Both the concentration dependence and seeding effect have been shown to occur in *in vitro* holo hSOD aggregation, indicating that holo hSOD aggregates via a nucleation-dependent process ((77) and Y. M. Hwang unpublished data). However, the specific pathways and mechanisms by which aggregation occurs are still being elucidated. In this chapter, aggregation of dimer interface mutants in the holo form are monitored using DLS.

The graph shows Mean light scattering intensity (kcps) on the y-axis versus Time (hours) on the x-axis, with the following labels:

y_f

y_i

$k_{app} = \dfrac{1}{\tau}$

$$Y = y_f + \frac{y_i - y_f}{1 + exp\left[\frac{(x - x_o)}{\tau}\right]}$$
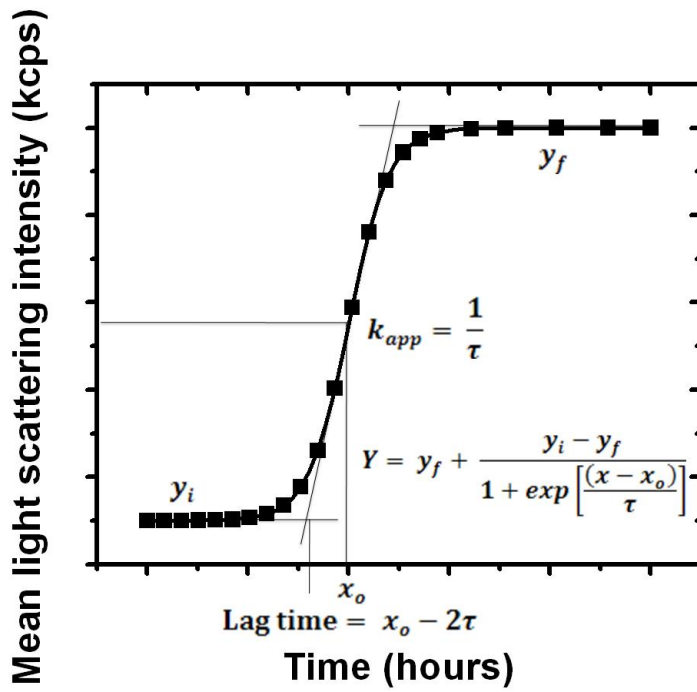
x_o

Lag time $= x_o - 2\tau$

Figure 4.2 A graphical representation of the sigmoidal increase in mean light scattering intensity upon aggregate formation (reproduced from (105)).

4.2 Methods

4.2.1 Expression and purification of recombinant holo hSOD

Protein expression and purification were performed as described in Section 3.2.1 and 3.2.2.

4.2.2 Protein quantification and confirmation of metal status

Protein quantification was performed as described in Section 3.2.4. The metallation status and sample quality were determined by the specific activity as well as DSC as described in Section 3.2.5.

4.2.3 DLS sample preparation

Holo hSOD aggregation protocols previously described in the thesis of Dr. Peter Stathopulos were used to study the fALS-associated hSOD mutant aggregation (77). Briefly, samples were prepared in 20 mM HEPES pH 7.8 buffer and aggregation was followed using light scattering as samples were incubated at 37 °C without agitation. All samples were prepared at a protein concentration of 10 mg/mL, unless stated otherwise, and were filtered using 20 nm filters (Anotop 10 Plus, Whatman) to remove any dust particles and preformed aggregates that may be present in the sample. Light scattering measurements were made using a 90Plus Particle Sizer (Brookhaven Instruments Corporation, Holtzville, NY) and a Nano-ZS Zetasizer (Malvern Instruments Ltd., Worcestershire, United Kingdom) in a 45 μL small volume cell (Quartz precision cell, type 105.251-QS, Hellma GmbH and Co., Mullheim, Germany). Samples were gently pipetted prior to transfer into the cell and measurements were made twice a day during the lag phase, 3 times a day during the exponential phase and once a day during the plateau phase.

The aggregation profiles obtained from both instruments agree well and, to avoid redundancy, only aggregation time courses from the 90Plus Particle Sizer will be presented.

4.2.4 Determining lag time from fits to a sigmoidal function

The kinetics of holo hSOD aggregation were fit using Microcal Origin 5.0 to an empirical sigmoidal function given by the following equation (also shown in Figure 4.2) (105):

$$Y = y_f + \frac{y_i - y_f}{1 + exp\left[\frac{(x - x_o)}{\tau}\right]}$$
Equation 4.5

where Y is the light scattering intensity (kcps); x is time and x_o is the time to half completion; y_i is the initial light scattering intensity; y_f is the final light scattering intensity; and τ is the time constant which is the reciprocal of the apparent rate constant for the growth phase of the curve ($1/k_{app}$). Although specific kinetic schemes cannot be obtained from the sigmoidal fit, it will provides a way to quantitatively compare the aggregation profiles of the different hSOD mutants. The lag time (duration of the lag phase) of the aggregation curve can be calculated from the fitted parameters using the following equation:

$$\text{Lag time} = x_o - 2\tau$$
Equation 4.6

4.2.5 Fitting holo hSOD aggregation profiles to a primary and secondary nucleation function

Protein aggregation can occur through primary or secondary nucleation, where primary nucleation describes elongation occurring only at the polymer ends while secondary nucleation implies the formation of new polymer ends through fragmentation, branching or heterogeneous nucleation (104). DLS data of holo fALS-associated hSOD mutant proteins were fit to both primary and secondary nucleation functions to determine which nucleation pathway holo fALS-

associated hSOD mutations undergo. Based on protein aggregation kinetics described by Ferrone (104), the aggregation profile for primary-nucleation will fit to a cosine function:

$$\text{fraction of completion} = A[1 - \cos(Bt)] \qquad \text{Equation 4.7}$$

where A is the fitted amplitude, B is the effective rate constant and t is time. On the other hand, the aggregation profile for secondary nucleation will fit a cosh function:

$$\text{fraction of completion} = A[\cosh(Bt) - 1] \qquad \text{Equation 4.8}$$

These fits are only applicable to the initial phase of the aggregation process, therefore, the aggregation profiles of hSOD were converted to fraction of completion and only the first 20% of the profiles were fit.

4.3 Acknowledgements

4.4 Results

4.4.1 Holo hSOD aggregation is nucleation dependent

A nucleation dependent aggregation process contains a rate limiting step associated with the formation of a critical nucleus. This process is characterized by the lag phase in an aggregation profile. The addition of preformed aggregates should decrease the lag phase since the critical nucleus is added. Figure 4.3 shows the aggregation profiles of 3 mg/mL holo pWT with and without the addition of preformed seeds. The seeds were obtained from a previous 3 mg/mL holo pWT time course with the early seeds collected at the end of the lag phase and the

late seeds collected at the plateau phase. The lag phase of holo pWT is reduced from 200 h to 28 h by the addition of early seeds and completely eliminated by the addition of late seeds, demonstrating that holo hSOD aggregation is nucleation dependent. These results agree with and confirm previous results obtained for other holo hSOD variants (77) (Y.M. Hwang unpublished data).
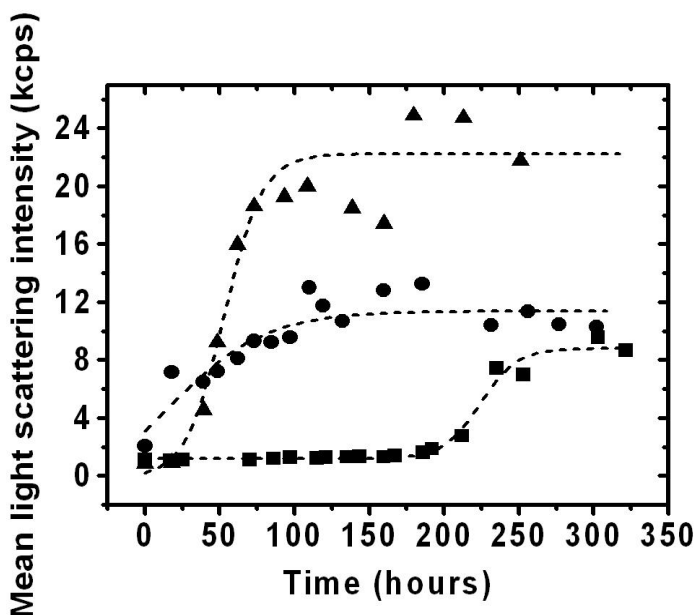
Figure 4.3 Nucleation dependence of holo hSOD aggregation. Aggregation profiles of 3 mg/mL holo pWT with 5% (v/v) early seeds (triangles), 5% (v/v) late seeds (circles) and without seeds (squares). The dashed lines are fits to an empirical sigmoidal function (Equation 4.5).

4.4.2 Dimer interface mutants A4S and A4T have shorter lag times compared to pWT

The aggregation profiles of dimer interface mutants A4S and A4T as well as pWT in the holo state were fit to Equation 4.5 and the lag times were determined from the fitted parameters using Equation 4.6. Table 4.1 summarizes the lag times and fitted parameters of the holo aggregation profiles. Aggregation profiles with fitted initial mean light scattering intensities, y_i,

65

that did not match experimental initial mean light scattering intensities were considered "pre-seeded" and were not included in the lag time determination. Figure 4.4 illustrates the aggregation profiles for pre-seeded and a non pre-seeded (successful) holo pWT samples. The experimental initial mean light scattering intensities of both profiles are approximately 2.6 kcps, however, the fitted initial light scattering intensities of the pre-seeded and non pre-seeded time courses are -14.10 kcps and 2.66 kcps, respectively. The lower than expected fitted initial light scattering intensity as well as the absence of an appreciable lag phase indicates that the sample contains some preformed aggregates, perhaps as an artefact from filtering.
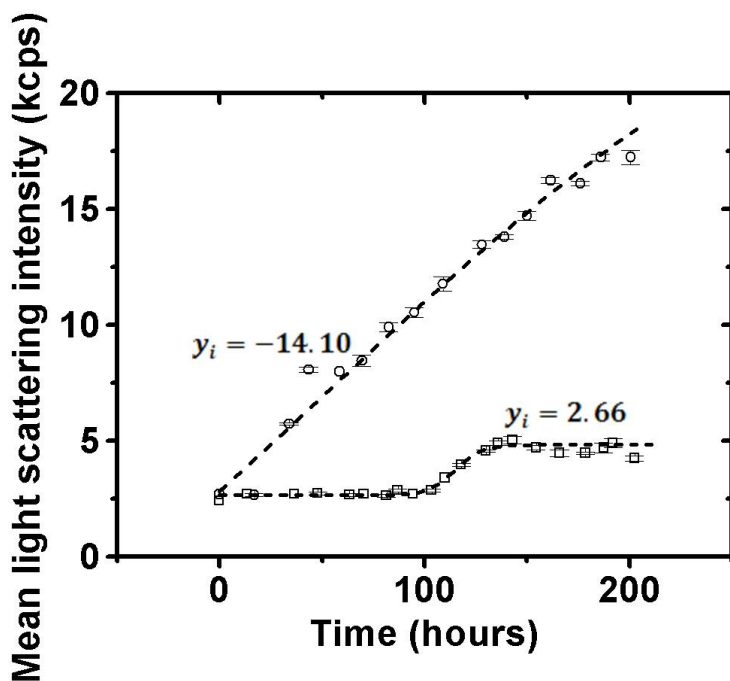
Figure 4.4 Pre-seeded and non pre-seeded 10 mg/mL holo pWT aggregation profiles. The pre-seeded data points are in open circles while the non pre-seeded data points are in open squares. The dashed lines are fits to Equation 4.5. The initial mean light scattering intensities,y_i, of the pre-seeded and non pre-seeded sample are -14.10 kcps and 2.66 kcps, respectively.

Protein aggregation studies have shown that the combination of adsorption to hydrophobic interfaces (filter membrane or air-water interface) and the shear stress associated

with the filtering process could exacerbate protein unfolding (106,107), which can lead to the formation of aggregation nucleus. However, light scattering data from multiple holo hSOD samples, prepared is a consistent manner, indicate that most of the samples are not pre-seeded and the sample solution at the beginning of the time course as well as during the lag phase is in fact monodispersed. Figure 4.5 is a representative intensity plot of a holo aggregation sample over time. At t=0 h throughout the lag phase, the solution is monodispersed with a particle size of ~5 nm, consistent with the size of hSOD dimer (77). As aggregation occurs, a larger species of ~1000nm appears.
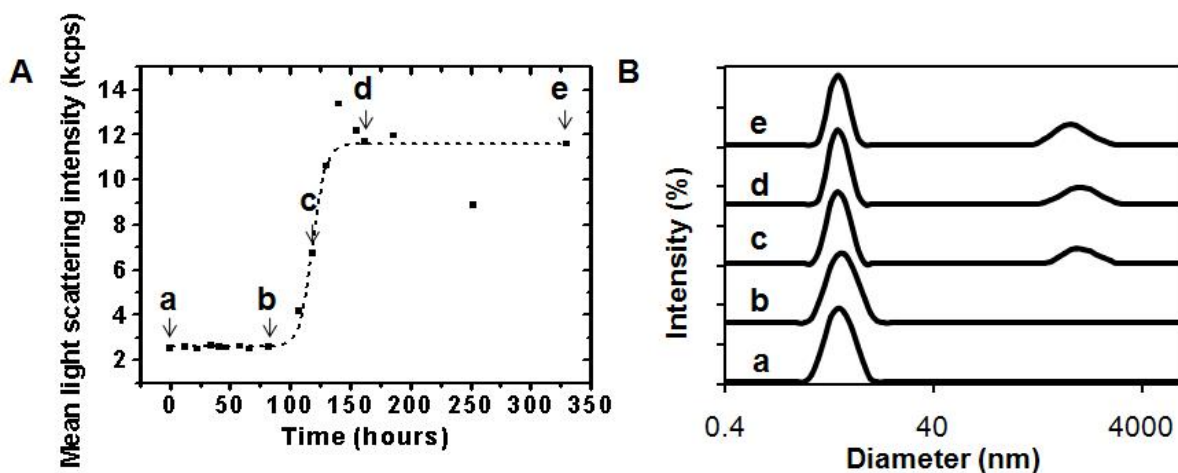
Figure 4.5 Size distribution of holo hSOD aggregation over time. (A) Aggregation profile of holo A4T with experimental data in solid squares and sigmoidal fit in dashed lines. (B) Intensity plots at different time points corresponding to points indicated in (A) for holo A4T aggregation.

Aggregation of holo hSOD samples are quite variable with varying lengths of lag times, growth phases and final mean light scattering intensities. This variability can be observed in Figure 4.6. Nevertheless, Figure 4.6 (D) and Table 4.1 show that the dimer interface mutants A4S and A4T appear to have shorter average lag times compared to pWT. The average lag time of A4T, 77.70±19.04 h, is clearly shorter than pWT, 135.28±28.48 h, while the averaged lag

time of A4S, 109.41±82.53 h, is slightly shorter than pWT. In Figure 4.6 (B), the aggregation profiles in blue and red (indicated by arrows) are from a single holo A4S sample that was split into two samples at the beginning of the experiment. However, they do not have similar lag times or final mean light scattering intensities, indicating that the variation between samples are not due to differences in sample quality but is intrinsic to hSOD aggregation.
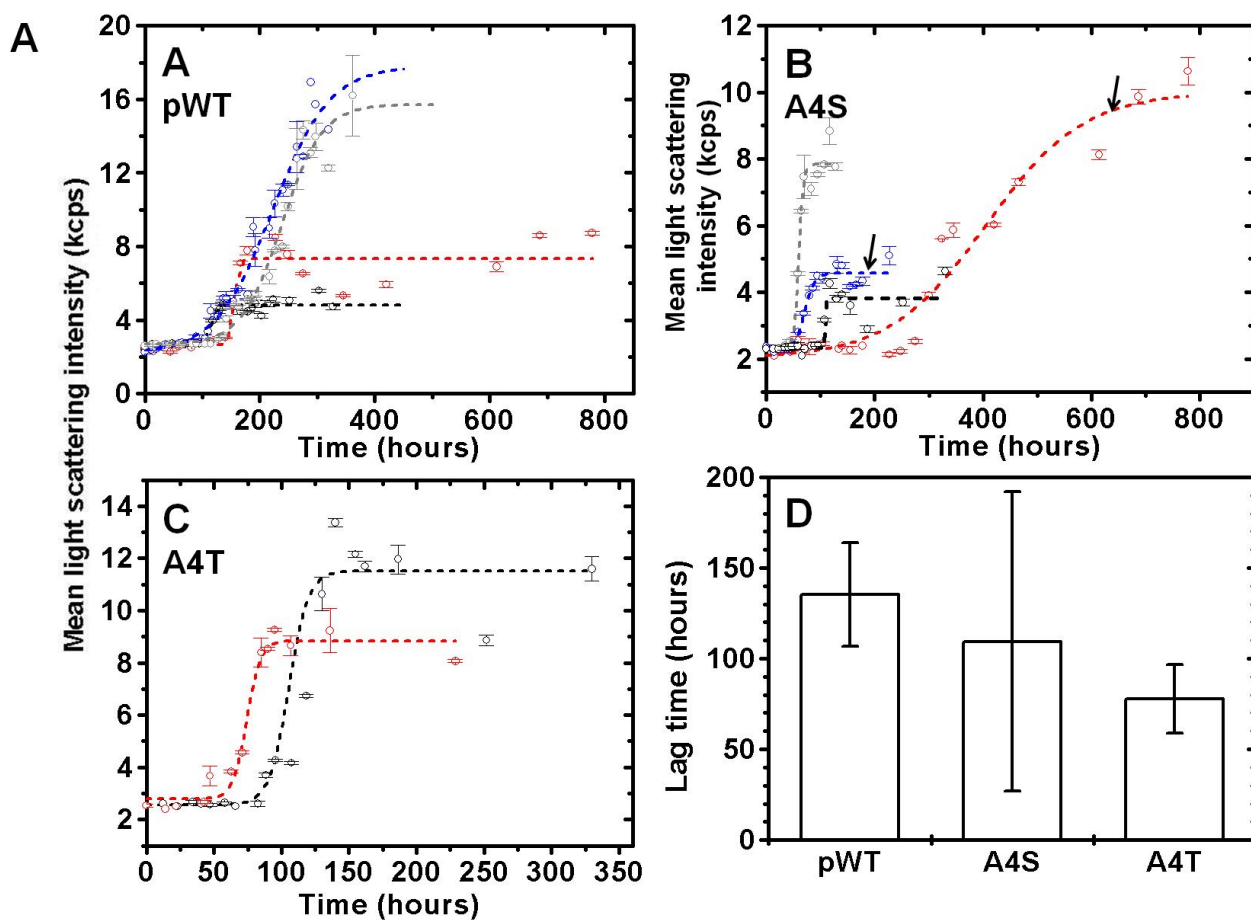
Figure 4.6 Aggregation profiles of holo dimer interface mutants and pWT. Experimental data for pWT (A), A4S (B) and A4T(C) are in hollow circles while the fits to Equation 4.5 are in dotted lines. (D) Bar graph of the average and standard deviation of fitted lag times reflect the variability in holo hSOD aggregation. A sample of holo A4S was divided into two identical fractions and monitored in parallel. The arrows indicate the aggregation profiles for the two holo A4S samples, which are in red and blue.

Table 4.1 Summary of holo hSOD aggregation fitted parameters to Equation 4.5.

Holo hSOD	Initial mean light scattering intensity (kcps) [a]	Final mean light scattering intensity (kcps) [a]	x_o (hrs) [a]	τ (hrs) [a]	lag time (hrs) [b]
pWT	2.19±0.48	17.82±1.77	222.19±12.94	49.69±9.42	122.82±16.01
pWT	2.68±0.29	15.73±0.86	237.90±6.74	34.78±5.26	168.34±8.55
pWT	2.66±0.09	4.83±0.08	115.11±2.43	6.09±2.18	102.93±3.27
pWT	2.65±0.30	7.33±0.30	155.29±3.20	4.13±4.22	147.04±5.30
pWT	*-14.10±12.24*	*29.11±1.77*	*57.30±66.90*	*130.71±34.11*	*-204.12±75.10*
			Mean±S.D.		135±28
A4S	2.33±0.10	3.83±0.13	107.44±0.00	0.26±0.00	106.93±0.00
A4S	2.37±0.23	7.84±0.20	60.07±1.26	4.09±1.27	51.89±1.79
A4S	2.26±0.15	4.57±0.10	70.39±3.25	9.25±2.76	51.88±4.26
A4S	2.03±0.27	10.00±0.53	405.09±21.58	89.08±20.25	226.93±29.59
			Mean±S.D.		109±82
A4T	2.79±0.23	8.85±0.27	74.29±2.04	5.03±1.55	64.23±2.57
A4T	2.57±0.33	11.52±0.39	105.33±8.12	7.08±4.62	91.16±9.34
A4T	*-33.78±77.68*	*18.28±1.93*	*-101.11±345.25*	*140.31±76.10*	*-381.73±353.53*
			Mean±S.D.		78±19

NOTE: All samples were at a protein concentration of 10 mg/mL in 20 mM HEPES pH 7.8 and incubated at 37 °C without agitation. Datasets in italics are from preseeded aggregation profiles and are excluded from average lag time considarations.

[a] Errors obtained from fitting program.

[c] Errors derived using standard procedures (84) from errors in fitted x_o and τ obtained from fitting program.

4.4.3 Holo hSOD aggregation proceeds via a secondary nucleation mechanism

Protein aggregation can proceed via a primary or secondary nucleation process (104). Secondary-nucleated aggregation has a distinctively steeper initial growth phase compared to primary-nucleated aggregation which has a more gradual initial growth phase. Figure 4.7 illustrates fits to both the primary and secondary nucleation models for pWT (A), A4S (B) and A4T(C) and shows that pWT, A4S and A4T, like other variants of holo hSOD (77) (Y. M. Hwang unpublished data), fit well to the secondary-nucleation equation (Equation 4.8). The fits to the primary-nucleation equation (Equation 4.7) have a more gradual growth compared to the fits to the secondary-nucleation equation and consistently deviate from the experimental data.
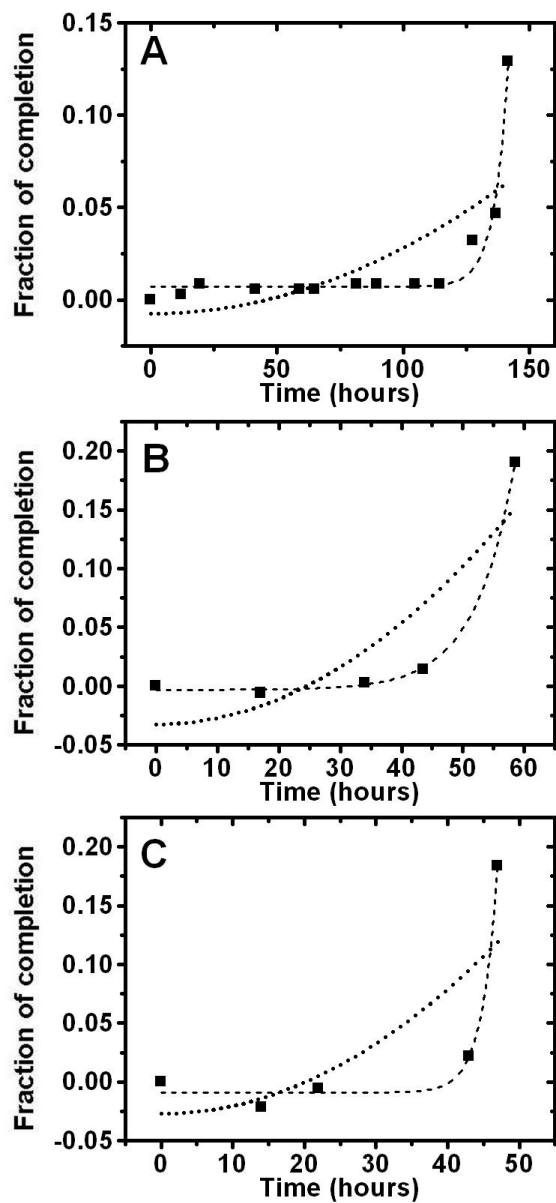
Figure 4.7 Holo aggregation fits to primary and secondary nucleation equations of pWT (A), A4S (B) and A4T (C). The solid squares are experimental data points while the dotted and dashed lines are the primary and secondary nucleation fits, respectively.

4.5   Discussion

4.5.1   Aggregates arise from holo hSOD dimer interface mutants A4S and A4T at physiologically relevant pH and temperature

A protein concentration of 10 mg/mL (317 μM) was used as it is within the estimated range of hSOD concentration in motor neurons as well as a pragmatic solution for shortening the long lag times observed during holo aggregation experiments. As mentioned in Section 4.1.2, concentration dependence is a feature of nucleation-dependent protein aggregation, therefore, higher protein concentrations will result in shorter lag times. Kurobe *et al.* and Bowling *et al.* reported hSOD concentrations in erythrocyte lysate to be 0.95±0.07 μg/mg haemoglobin and 7.0±1.8 μg/mg of protein, respectively (108,109), which correlates to hSOD concentrations of ~10 μM and 76 μM, respectively (based on normal mean corpuscular haemoglobin concentrations of 320 g/L, also assuming haemoglobin is ~total amount of protein in RBC). It has also been reported that the concentration of hSOD in brain is ~4.5 times higher than in erythrocytes, corresponding to hSOD concentrations of ~45-340 μM (100,109). Moreover, immunohistochemical studies indicate that motor neurons have higher concentrations of hSOD compared to other neuronal populations (110). Although other studies on hSOD aggregation rarely have protein concentrations above 3.15 mg/mL (100 μM) (90,100), there are various protein aggregation studies of other proteins that use protein concentrations in the range of 10 mg/mL (111-114).

The pWT and dimer interface mutants A4S and A4T used in the holo aggregation experiments were fully metallated as confirmed by the pyrogallol activity assay and DSC. The full metallation status of hSOD was characterized by having a specific activity of 1800±200

U/mg and a single endothermic peak by DSC (Figure 3.3 C and D). The correlation of this specific activity range to a full metallation status was previously confirmed with inductively coupled plasma atomic emission spectroscopy (ICP-AES) where holo hSOD samples with specific activities of 1800±200 U/mg had Cu^{2+} and Zn^{2+} to monomer ratios of ~1 (77). The average specific activities for A4S and A4T are 1943±63 U/mg and 1736±260 U/mg, respectively; this, together with the single peak observed in DSC indicates that the mutants are fully metallated. Additionally, if aggregation occurred from a small amount of apo/mismetalated or misfolded protein in the sample, not only should the specific activity of the sample increase as aggregation occurs but aggregation should not restart after the aggregates are removed at the plateau phase, since both should affectively remove the apo/mismetalated/misfolded hSOD that may be present initially. Previous studies on holo hSOD aggregation have shown that the specific activity of the sample decreases with time while samples from restart experiments, where samples at plateau phase were filtered using 20 nm filters to remove the aggregates, go through another sigmoidal aggregation profile (Y. M. Hwang unpublished data). These indicate that the observed aggregation profiles are not due to pre-existing apo/mismetallated or midfolded hSOD in the sample but arise from holo hSOD.

Despite several studies reporting that holo hSOD does not aggregate at physiologically relevant conditions (37,90), we observe that holo A4S and A4T, in addition to other holo hSOD mutants studied in the Meiering laboratory ((77) and Y.M. Hwang unpublished data), do possess the ability to aggregate at physiologically relevant conditions of pH 7.8, 37 °C and without agitation. This discrepancy could be due to differences in experimental conditions. Thioflavin T (ThT) dye binding was employed in the previous studies to monitor hSOD aggregation (90,91) while our studies use light scattering to directly measure the change in particle size in solution.

ThT is an amyloid specific dye that binds to the surface of the β-rich quaternary structure of amyloid fibrils (115). It is worth noting that the aggregates formed in our holo aggregation studies as well as in ALS patients are not amyloid and do not exhibit the classical features of amyloid, such as long unbranched fibrils, ThT binding, in the case of our aggregates (Y. M. Hwang unpublished data), and green-gold birefringence when stained with Congo red, in the case of protein inclusions in ALS patients (11,116). It is also important to note that dye binding assays have an inherent shortcoming in that the addition of the dyes may affect the equilibrium between the various protein states in the sample (98). Another difference could be the shorter range of time the samples are monitored for or a lower frequency of measurements in the previous studies compared to the long time courses in our experiments. Identical holo hSOD samples, monitored concomitantly, revealed that samples that were measured more frequently have shorter lag times compared to those that were not (Y. M. Hwang unpublished data), suggesting that the sample measurement process promotes aggregation. To minimize any inconsistencies from the measurement process, the frequency of measurements was done in a consistent manner (described in Section 4.2.3) for all samples.

4.5.2 Holo hSOD dimer interface mutants A4S and A4T have shorter lag times compared to pWT

Dimer interface mutants A4S and A4T have shorter averaged lag times compared to pWT. This is in agreement with previous data obtained in the Meiering laboratory where dimer interface mutants A4V and I149T also have shorter lag times compared to pWT (77) (Y.M. Hwang unpublished data). However, non-dimer interface mutants G93A/D/R/S/V, with the exception of G85R which has an averaged lag time of ~97 h, have average lag times similar to, if not longer than, pWT (77,91) (Y.M. Hwang unpublished data). G85R is a mutation that disrupts

metal binding. This implies that a disrupted dimer interface and/or metal binding increases the aggregation propensity of holo hSOD and, perhaps, monomerization may be involved in aggregation. Monomerization is not an uncommon step in the protein aggregation pathways of multisubunit proteins and occurs during the aggregation of transthyretin (117) and insulin (118). It has also been shown that the majority of hSOD mutations either decrease dimer stability or increase dimer disscociation (36). In addition, studies using an antibody specific to the dimer interface of hSOD have shown that aggregates in mice models and in an A4V patient contain dimer interface exposed species (52,119). Therefore, it is reasonable to conclude that hSOD aggregation can proceed via monomerization or partial exposure of the dimer interface.

The lag times also correlate with the thermodynamic stability of A4S and A4T. A4S has higher thermal stability compared to A4T while both mutants are destabilized compared to pWT (Chapter 3). Alanine 4 is located at the edge of the dimer interface and points into the core of the β-barrel. Both A4S and A4T replace a non-polar residue with a more polar residue and are also both larger compared to alanine. Both the decrease in hydrophobicity and increase in side chain size will likely weaken the dimer interface and destabilize the monomer. As discussed in Chapter 3, ITC of holo hSOD mutants indicate that dimer dissociation of hSOD mutants, G93A/D/R, were only mildly weaker compared to pWT, while dimer interface mutants, A4V and I113T, much weaker with K_ds of 48 μM and 33 μM, respectively (77). DSC and ITC experiments on apo hSOD mutants also indicate that hSOD mutants, G93S, A4V, A4S, A4T, I113T, H43R (arranged from high to low stability), have decreased monomer stability compared to pWT (79), while chemical denaturation studies on both apo and holo hSOD mutants, G85R and E100G, indicate that monomer stability is comparably compromised in both states (68,72,78). G85R also has weakened metal binding. This is interesting because G85R was the only non-dimer interface

mutant with an appreciably shorter lag time compared to pWT (77) (Y. M. Hwang unpublished data). The destabilization of the dimer interface and/or weakened metal binding combined with decreased monomer stability may account for the increased aggregation propensity of dimer interface mutants A4S, A4T, A4V and mostly likely I149T as well as G85R. The shorter lag time for A4T compared to A4S also agrees with patient duration data where the average duration for A4T is 1.5 (n=21) years while A4S is >3 (n=1) years (64). However, it is important to note that correlation between stability and aggregation propensity with disease duration is not well defined.

4.5.3 Multiple pathways of aggregation

It is worth noting that there is much variability in the aggregation profiles for each hSOD variant in terms of lag times, final mean scattering intensities and growth rates. It is generally accepted that protein aggregation is a complex process in which many competing reactions and possibly different mechanisms may occur simultaneously. It is also known that the same peptide or protein can form aggregates with different morphologies, possibly undergoing different mechanisms/pathways, depending on differences in experimental conditions and the initial state of the protein (98,120). An obvious possible cause and concern with regards to the variations observed in our studies are variations between sample preparations such as metal content or minor differences in protein/buffer concentrations. However, samples that have been split into two and measured concurrently have produced aggregation profiles that are quite different, as illustrated in Figure 4.6 (B). This difference in aggregation profiles of identical samples has also been observed in previous studies (Y. M. Hwang unpublished data), suggesting that the variations between samples are not due to differences in protein/sample quality but is intrinsic to hSOD aggregation.

ALS patient as well as cell model studies reveal varying fine structures of aggregates, from filaments of varying diameters and granule-coated fibrils to soluble aggregates (12,13). In addition, due to the inability to differentiate between the different secondary-nucleation mechanisms (fragmentation, branching, heterogeneous), we cannot preclude the possibility that the variations in the aggregation profiles within each hSOD variant is due to the different samples undergoing different combinations of aggregation pathways that lead to slightly different aggregate distributions, thus resulting in different aggregation rates and final mean intensities. Additionally, AFM of holo aggregation samples at the plateau phase do show aggregates of different morphologies (Y. M. Hwang unpublished data).

Chapter 5 Summary and future work

5.1   Production of recombinant fALS-associated mutants

In order to produce fALS-associated hSOD mutants in *E. coli*, the mutations of interest were introduced into the recombinant pHSOD1ASlacI^q vector that encodes pWT hSOD. Using the pWT background allows quantitative thermodynamic analyses of the ALS-associated mutants to be carried out. This is due to the lack of free cysteines in the pWT construct that enables the reversible thermal and chemical unfolding. Seven ALS associated mutations here were successfully introduced the pWT background via PCR-site directed mutagenesis. Those mutants are dimer interface mutants, A4S, A4T, V148G and V148I, metal binding mutant H80R as well as charge mutants, G37R and G41D. Of these mutants, A4S and A4T were extensively characterized while some preliminary data was obtained for G41D and H80R.

The mutations H48R, N86D and I112T were not successfully introduced despite several attempts to do so. However, designing new primers may increase the efficiency of the PCR-site directed mutagenesis. I112T is a dimer interface mutation while H48R is a copper binding mutant. On the other, like G41D, N86D is one of the few mutations that increase the net negative charge of hSOD. These mutations, including the ones that were successfully obtained, are structurally and chemically diverse, with disease durations ranging from 0.9 years to 14.1 years (32,63-66). Characterization of their biophysical properties will shed more light on the mechanisms in which ALS-associated hSOD mutants infer toxicity.

5.2 Thermal stability of ALS-associated hSOD mutants

DSC was used to determine the thermal stability of dimer interface mutants A4S, A4T and I113T as well as G41D compared to pWT in the holo state. All 3 dimer interface mutant were destabilized compared to pWT, which is similar to findings for other holo hSOD mutants (28,71)((72) Chapter 4) ((73) Chapter 2). The mutants studied here are well fit by a dimer 2-state unfolding model and the dimer interface mutants exhibit protein concentration dependence characteristic of dimer 2-state unfolding at lower protein concentrations, with somewhat less stabilization than expected at increased protein concentration, perhaps due to increased aggregation. The dimer interface mutants had $\Delta H_{vH}/\Delta H_{cal}$ ratios of slightly less than one, which suggestive of formation of a monomer intermediate. Fits to a monomer 2-state unfolding model exhibit systematic deviations from the experimental data, as was also observed for monomer 2-state fits of holo pWT (28); this rules out unfolding via a monomer 2-state mechanism. However, the low $\Delta H_{vH}/\Delta H_{cal}$ ratios in addition evidence of a monomer intermediate from ITC and chemical denaturation experiments of other mutants in the holo and apo states suggests that holo A4S, A4T and I 113T may also have a weakened dimer interface.

Preliminary data on H80R indicate that the mutant has comparable stability to pWT in the apo state. However, the as isolated H80R T_m of ~60 °C was only 1 °C higher than apo H80R, indicating that either H80R does not have any bound metals or it is only slightly stabilized by metal binding. All batches of purified H80R contained fragments of 7.2 kDa and 8.6 kDa in size. These fragments were found to correspond to the protein being cleaved between R69 and K70. The mechanism of cleavage is still unknown. The two most likely mechanisms are aberrant copper chemistry, which has been observed for mutant hSOD (40,53) or an enhanced susceptibility to proteolysis.

5.2.1 Future work

All 3 dimer interface mutants have lower than predicted T_m at higher protein concentrations (Figure 3.4). However, there are very few data points at higher protein concentrations. To determine if the T_ms of the mutants really fall below the predicted concentration dependence, more DSC scans should be performed at higher protein concentrations. The data should also be fit to a 3-state monomer intermediate unfolding model as there is precedence that the dimer interfaces of A4S, A4T and I113T are destabilized compared to pWT, in both the holo and the apo forms of the proteins (28,68,72,73,77-79). This will allow comparisons of population distribution between the mutants and pWT. ITC experiments on the holo dimer interface mutants could provide more information regarding the the strength of the dimer interface. It has previously been shown that ITC of holo I113T at 65 °C gives heats of dissociation that can be used to determine the K_d (77). Since I113T has comparable $\Delta H_{vH}/\Delta H_{cal}$ ratios and T_m values to A4S and A4T in DSC in the holo form, it is likely that the K_ds of holo A4S and A4T can be determined using ITC.

Due to the similarity in T_m of the as isolated and apo H80R, the metal content of this variant should be verified using another technique, e.g. using ICP-AES. Information from metal analysis could provide more insight to the mechanism of H80R fragmentation as the presence of copper is required for aberrant chemistry to occur. Depending on the cause of the protein cleavage, a modified protein purification protocol can then be developed to obtain non-cleaved H80R for further analysis.

5.3   Aggregation propensity of dimer interface mutants in the holo state

Holo forms of the dimer interface mutants A4S and A4T aggregate via a secondary-nucleation mechanism. This is contradictory to studies that claim holo hSOD is too stable to aggregate (89). The lag times of the mutants were quantitatively determined by fitting the aggregation profiles to an empirical sigmoidal function. The lag times for the mutants are shorter than for pWT with A4T having a greater decrease in lag time compared to A4S. This correlates with the stability of the mutants determined using DSC where A4T is more thermally destabilized than A4S, while both mutants were destabilized compared to pWT. The shorter lag times of dimer interface mutants (A4S, A4T, A4V and I149T) compared to pWT and non-dimer interface mutants suggests that a weakened dimer interface increases aggregation propensity. However, aggregation experiments on various holo hSOD variants in the Meiering lab clearly indicate that aggregation can arise from this form of the protein. Also, the ability of holo pWT to aggregate at physiological pH and temperature and without agitation suggests a possible connection between fALS and sALS.

5.3.1 Future work

Long term objectives of the holo aggregation studies include determining the effects of many different types of hSOD mutations on aggregation propensity and elucidation of the mechanism(s) by which aggregation occurs. An interesting avenue to pursue is the charge mutations such as G37R and G41D to further investigate the effects of decreasing or increasing the overall net charge of the protein. So far, G85R is the only mutant studied in our laboratory that has comparable lag times to dimer interface mutants. The other non-dimer interface mutants appear to have lag times similar to if not longer than pWT (Y. M. Hwang unpublished data).

Aggregation of holo hSOD can be compared to aggregation of other forms of hSOD as well as other natively folded proteins that aggregate and cause disease. This should provide valuable insights into fundamental aspects of aggregation mechanisms, and contribute to understanding the toxic nature of protein aggregation in ALS and other PCDs.

References

1.   Gregersen N, Bolund L, Bross P. Protein misfolding, aggregation, and degradation in disease. Mol Biotechnol 2005;31(2):141-50.
2.   Chiti F, Dobson CM. Protein misfolding, functional amyloid, and human disease. Annu Rev Biochem 2006;75:333-66.
3.   Murphy RM, Kendrick BS. Protein misfolding and aggregation. Biotechnol Prog 2007;23(3):548-52.
4.   Kendrick BS, Cleland JL, Lam X, Nguyen T, Randolph TW, Manning MC, Carpenter JF. Aggregation of recombinant human interferon gamma: kinetics and structural transitions. J Pharm Sci 1998;87(9):1069-76.
5.   Glabe CG. Common mechanisms of amyloid oligomer pathogenesis in degenerative disease. Neurobiol Aging 2006;27(4):570-5.
6.   Frid P, Anisimov SV, Popovic N. Congo red and protein aggregation in neurodegenerative diseases. Brain Res Rev 2007;53(1):135-60.
7.   Sipe JD, Cohen AS. Review: history of the amyloid fibril. J Struct Biol 2000;130(2-3):88-98.
8.   Westermark GT, Johnson KH, Westermark P. Staining methods for identification of amyloid in tissue. Methods Enzymol 1999;309:3-25.
9.   Meredith SC. Protein denaturation and aggregation: Cellular responses to denatured and aggregated proteins. Ann N Y Acad Sci 2005;1066:181-221.
10.   Rochet JC, Lansbury PT, Jr. Amyloid fibrillogenesis: themes and variations. Curr Opin Struct Biol 2000;10(1):60-8.
11.   Okamoto K, Hirai S, Yamazaki T, Sun XY, Nakazato Y. New ubiquitin-positive intraneuronal inclusions in the extra-motor cortices in patients with amyotrophic lateral sclerosis. Neurosci Lett 1991;129(2):233-6.
12.   Murayama S, Mori H, Ihara Y, Bouldin TW, Suzuki K, Tomonaga M. Immunocytochemical and Ultrastructural Studies of Lower Motor Neurons in Amyotrophic Lateral Sclerosis. Annals of Neurology 1990;27(2):137-148.
13.   Matsumoto G, Stojanovic A, Holmberg CI, Kim S, Morimoto RI. Structural properties and neuronal toxicity of amyotrophic lateral sclerosis-associated Cu/Zn superoxide dismutase 1 aggregates. J Cell Biol 2005;171(1):75-85.
14.   Kato S, Takikawa M, Nakashima K, Hirano A, Cleveland DW, Kusaka H, Shibata N, Kato M, Nakano I, Ohama E. New consensus research on neuropathological aspects of familial amyotrophic lateral sclerosis with superoxide dismutase 1 (SOD1) gene mutations: inclusions containing SOD1 in neurons and astrocytes. Amyotroph Lateral Scler Other Motor Neuron Disord 2000;1(3):163-84.
15.   Logroscino G, Traynor BJ, Hardiman O, Chio A, Couratier P, Mitchell JD, Swingler RJ, Beghi E. Descriptive epidemiology of amyotrophic lateral sclerosis: new evidence and unsolved issues. J Neurol Neurosurg Psychiatry 2008;79(1):6-11.
16.   Julien JP. ALS: astrocytes move in as deadly neighbors. Nat Neurosci 2007;10(5):535-7.
17.   Miller RG, Mitchell JD, Lyon M, Moore DH. Riluzole for amyotrophic lateral sclerosis (ALS)/motor neuron disease (MND). Amyotroph Lateral Scler Other Motor Neuron Disord 2003;4(3):191-206.
18.   Gutmann L, Mitsumoto H. Advances in ALS. Neurology 1996;47(4 Suppl 2):S17-8.

19. Valentine JS, Doucette PA, Zittin Potter S. Copper-zinc superoxide dismutase and amyotrophic lateral sclerosis. Annu Rev Biochem 2005;74:563-93.

20. Orrell RW. Amyotrophic lateral sclerosis: copper/zinc superoxide dismutase (SOD1) gene mutations. Neuromuscul Disord 2000;10(1):63-8.

21. Rosen DR, Siddique T, Patterson D, Figlewicz DA, Sapp P, Hentati A, Donaldson D, Goto J, O'Regan JP, Deng HX and others. Mutations in Cu/Zn superoxide dismutase gene are associated with familial amyotrophic lateral sclerosis. Nature 1993;362(6415):59-62.

22. Pasinelli P, Brown RH. Molecular biology of amyotrophic lateral sclerosis: insights from genetics. Nat Rev Neurosci 2006;7(9):710-23.

23. Boillee S, Vande Velde C, Cleveland DW. ALS: a disease of motor neurons and their nonneuronal neighbors. Neuron 2006;52(1):39-59.

24. Hallewell RA, Imlay KC, Lee P, Fong NM, Gallegos C, Getzoff ED, Tainer JA, Cabelli DE, Tekamp-Olson P, Mullenbach GT and others. Thermostabilization of recombinant human and bovine CuZn superoxide dismutases by replacement of free cysteines. Biochem Biophys Res Commun 1991;181(1):474-80.

25. Andersen PM. Genetic factors in the early diagnosis of ALS. Amyotroph Lateral Scler Other Motor Neuron Disord 2000;1 Suppl 1:S31-42.

26. Figlewicz DA, Orrell RW. The genetics of motor neuron diseases. Amyotroph Lateral Scler Other Motor Neuron Disord 2003;4(4):225-31.

27. Bordo D, Djinovic K, Bolognesi M. Conserved patterns in the Cu,Zn superoxide dismutase family. J Mol Biol 1994;238(3):366-86.

28. Stathopulos PB, Rumfeldt JA, Karbassi F, Siddall CA, Lepock JR, Meiering EM. Calorimetric analysis of thermodynamic stability and aggregation for apo and holo amyotrophic lateral sclerosis-associated Gly-93 mutants of superoxide dismutase. J Biol Chem 2006;281(10):6184-93.

29. Koradi R, Billeter M, Wuthrich K. MOLMOL: a program for display and analysis of macromolecular structures. J Mol Graph 1996;14(1):51-5, 29-32.

30. Parge HE, Hallewell RA, Tainer JA. Atomic structures of wild-type and thermostable mutant recombinant human Cu,Zn superoxide dismutase. Proc Natl Acad Sci U S A 1992;89(13):6109-13.

31. Getzoff ED, Cabelli DE, Fisher CL, Parge HE, Viezzoli MS, Banci L, Hallewell RA. Faster superoxide dismutase mutants designed by enhancing electrostatic guidance. Nature 1992;358(6384):347-51.

32. Andersen PM, Sims KB, Xin WW, Kiely R, O'Neill G, Ravits J, Pioro E, Harati Y, Brower RD, Levine JS and others. Sixteen novel mutations in the Cu/Zn superoxide dismutase gene in amyotrophic lateral sclerosis: a decade of discoveries, defects and disputes. Amyotroph Lateral Scler Other Motor Neuron Disord 2003;4(2):62-73.

33. Andersen PM, Nilsson P, Ala-Hurula V, Keranen ML, Tarvainen I, Haltia T, Nilsson L, Binzer M, Forsgren L, Marklund SL. Amyotrophic lateral sclerosis associated with homozygosity for an Asp90Ala mutation in CuZn-superoxide dismutase. Nat Genet 1995;10(1):61-6.

34. Jonsson PA, Backstrand A, Andersen PM, Jacobsson J, Parton M, Shaw C, Swingler R, Shaw PJ, Robberecht W, Ludolph AC and others. CuZn-superoxide dismutase in D90A heterozygotes from recessive and dominant ALS pedigrees. Neurobiol Dis 2002;10(3):327-33.

35. Robberecht W, Aguirre T, Van den Bosch L, Tilkin P, Cassiman JJ, Matthijs G. D90A heterozygosity in the SOD1 gene is associated with familial and apparently sporadic amyotrophic lateral sclerosis. Neurology 1996;47(5):1336-9.

36. Khare SD, Caplow M, Dokholyan NV. FALS mutations in Cu, Zn superoxide dismutase destabilize the dimer and increase dimer dissociation propensity: a large-scale thermodynamic analysis. Amyloid 2006;13(4):226-35.

37. DiDonato M, Craig L, Huff ME, Thayer MM, Cardoso RM, Kassmann CJ, Lo TP, Bruns CK, Powers ET, Kelly JW and others. ALS mutants of human superoxide dismutase form fibrous aggregates via framework destabilization. J Mol Biol 2003;332(3):601-15.

38. Reaume AG, Elliott JL, Hoffman EK, Kowall NW, Ferrante RJ, Siwek DF, Wilcox HM, Flood DG, Beal MF, Brown RH, Jr. and others. Motor neurons in Cu/Zn superoxide dismutase-deficient mice develop normally but exhibit enhanced cell death after axonal injury. Nat Genet 1996;13(1):43-7.

39. Bruijn LI, Houseweart MK, Kato S, Anderson KL, Anderson SD, Ohama E, Reaume AG, Scott RW, Cleveland DW. Aggregation and motor neuron toxicity of an ALS-linked SOD1 mutant independent from wild-type SOD1. Science 1998;281(5384):1851-4.

40. Goto JJ, Gralla EB, Valentine JS, Cabelli DE. Reactions of hydrogen peroxide with familial amyotrophic lateral sclerosis mutant human copper-zinc superoxide dismutases studied by pulse radiolysis. J Biol Chem 1998;273(46):30104-9.

41. Wiedau-Pazos M, Goto JJ, Rabizadeh S, Gralla EB, Roe JA, Lee MK, Valentine JS, Bredesen DE. Altered reactivity of superoxide dismutase in familial amyotrophic lateral sclerosis. Science 1996;271(5248):515-8.

42. Yim HS, Kang JH, Chock PB, Stadtman ER, Yim MB. A familial amyotrophic lateral sclerosis-associated A4V Cu, Zn-superoxide dismutase mutant has a lower Km for hydrogen peroxide. Correlation between clinical severity and the Km value. J Biol Chem 1997;272(14):8861-3.

43. Liu R, Althaus JS, Ellerbrock BR, Becker DA, Gurney ME. Enhanced oxygen radical production in a transgenic mouse model of familial amyotrophic lateral sclerosis. Ann Neurol 1998;44(5):763-70.

44. Andrus PK, Fleck TJ, Gurney ME, Hall ED. Protein oxidative damage in a transgenic mouse model of familial amyotrophic lateral sclerosis. J Neurochem 1998;71(5):2041-8.

45. Beckman JS, Carson M, Smith CD, Koppenol WH. ALS, SOD and peroxynitrite. Nature 1993;364(6438):584.

46. Beal MF, Ferrante RJ, Browne SE, Matthews RT, Kowall NW, Brown RH, Jr. Increased 3-nitrotyrosine in both sporadic and familial amyotrophic lateral sclerosis. Ann Neurol 1997;42(4):644-54.

47. Ferrante RJ, Shinobu LA, Schulz JB, Matthews RT, Thomas CE, Kowall NW, Gurney ME, Beal MF. Increased 3-nitrotyrosine and oxidative damage in mice with a human copper/zinc superoxide dismutase mutation. Ann Neurol 1997;42(3):326-34.

48. Bruijn LI, Beal MF, Becher MW, Schulz JB, Wong PC, Price DL, Cleveland DW. Elevated free nitrotyrosine levels, but not protein-bound nitrotyrosine or hydroxyl radicals, throughout amyotrophic lateral sclerosis (ALS)-like disease implicate tyrosine nitration as an aberrant in vivo property of one familial ALS-linked superoxide dismutase 1 mutant. Proc Natl Acad Sci U S A 1997;94(14):7606-11.

49. Wang J, Slunt H, Gonzales V, Fromholt D, Coonfield M, Copeland NG, Jenkins NA, Borchelt DR. Copper-binding-site-null SOD1 causes ALS in transgenic mice: aggregates of non-native SOD1 delineate a common feature. Hum Mol Genet 2003;12(21):2753-64.

50. Shibata N, Asayama K, Hirano A, Kobayashi M. Immunohistochemical study on superoxide dismutases in spinal cords from autopsied patients with amyotrophic lateral sclerosis. Developmental Neuroscience 1996;18(5-6):492-498.

51. Shibata N, Hirano A, Kobayashi M, Siddique T, Deng HX, Hung WY, Kato T, Asayama K. Intense superoxide dismutase-1 immunoreactivity in intracytoplasmic hyaline inclusions of familial amyotrophic lateral sclerosis with posterior column involvement. Journal of Neuropathology and Experimental Neurology 1996;55(4):481-490.

52. Liu HN, Sanelli T, Horne P, Pioro EP, Strong MJ, Rogaeva E, Bilbao J, Zinman L, Robertson J. Lack of evidence of monomer/misfolded superoxide dismutase-1 in sporadic amyotrophic lateral sclerosis. Ann Neurol 2009;66(1):75-80.

53. Bruijn LI, Miller TM, Cleveland DW. Unraveling the mechanisms involved in motor neuron degeneration in ALS. Annu Rev Neurosci 2004;27:723-49.

54. Bruening W, Roy J, Giasson B, Figlewicz DA, Mushynski WE, Durham HD. Up-regulation of protein chaperones preserves viability of cells expressing toxic Cu/Zn-superoxide dismutase mutants associated with amyotrophic lateral sclerosis. J Neurochem 1999;72(2):693-9.

55. Lepock JR, Frey HE, Hallewell RA. Contribution of conformational stability and reversibility of unfolding to the increased thermostability of human and bovine superoxide dismutase mutated at free cysteines. J Biol Chem 1990;265(35):21612-8.

56. Bolivar F, Rodriguez RL, Greene PJ, Betlach MC, Heyneker HL, Boyer HW, Crosa JH, Falkow S. Construction and characterization of new cloning vehicles. II. A multipurpose cloning system. Gene 1977;2(2):95-113.

57. Hallewell RA, Laria I, Tabrizi A, Carlin G, Getzoff ED, Tainer JA, Cousens LS, Mullenbach GT. Genetically engineered polymers of human CuZn superoxide dismutase. Biochemistry and serum half-lives. J Biol Chem 1989;264(9):5260-8.

58. Steinman HM. Bacteriocuprein superoxide dismutase of Photobacterium leiognathi. Isolation and sequence of the gene and evidence for a precursor form. J Biol Chem 1987;262(4):1882-7.

59. Hallewell RA, Masiarz FR, Najarian RC, Puma JP, Quiroga MR, Randolph A, Sanchez-Pescador R, Scandella CJ, Smith B, Steimer KS and others. Human Cu/Zn superoxide dismutase cDNA: isolation of clones synthesising high levels of active or inactive enzyme from an expression library. Nucleic Acids Res 1985;13(6):2017-34.

60. Chen LL. Preparation and Characterization of Recombinant Human CuZn Superoxide Dismutase Causing Familial Amyotrophic Lateral Sclerosis [Ph. D.]. London, United Kingdom: Imperial College of Science, Technology and Medicine; 1998. 230 p.

61. Rezania K, Yan JH, Dellefave L, Deng HX, Siddique N, Pascuzzi RT, Siddique T, Roos RP. A rare Cu/Zn superoxide dismutase mutation causing familial amyotrophic lateral sclerosis with variable age of onset, incomplete penetrance and a sensory neuropathy. Amyotrophic Lateral Sclerosis and Other Motor Neuron Disorders 2003;4(3):162-166.

62. Andersen PM. Amyotrophic lateral sclerosis associated with mutations in the CuZn superoxide dismutase gene. Curr Neurol Neurosci Rep 2006;6(1):37-46.

63. Sato T, Nakanishi T, Yamamoto Y, Andersen PM, Ogawa Y, Fukada K, Zhou Z, Aoike F, Sugai F, Nagano S and others. Rapid disease progression correlates with instability of mutant SOD1 in familial ALS. Neurology 2005;65(12):1954-7.

64. Wang Q, Johnson JL, Agar NY, Agar JN. Protein aggregation and protein instability govern familial amyotrophic lateral sclerosis patient survival. PLoS Biol 2008;6(7):e170.

65. Alexander MD, Traynor BJ, Miller N, Corr B, Frost E, McQuaid S, Brett FM, Green A, Hardiman O. "True" sporadic ALS associated with a novel SOD-1 mutation. Ann Neurol 2002;52(5):680-3.

66. Sandelin E, Nordlund A, Andersen PM, Marklund SS, Oliveberg M. Amyotrophic lateral sclerosis-associated copper/zinc superoxide dismutase mutations preferentially reduce the repulsive charge of the proteins. J Biol Chem 2007;282(29):21230-6.

67. Orrell RW, Habgood JJ, Gardiner I, King AW, Bowe FA, Hallewell RA, Marklund SL, Greenwood J, Lane RJM, deBelleroche J. Clinical and functional investigation of 10 missense mutations and a novel frameshift insertion mutation of the gene for copper-zinc superoxide dismutase in UK families with amyotrophic lateral sclerosis. Neurology 1997;48(3):746-751.

68. Rumfeldt JAO, University of Waterloo. Dept. of Chemistry. Thermodynamics, kinetics and structural dynamics of amyotrophic lateral sclerosis-associated mutant copper-zinc superoxide dismutases [Thesis Ph D --University of Waterloo 2006]. Waterloo, Ont.: University of Waterloo; 2006. xix, 280 leaves p.

69. Miller JF. Bacterial transformation by electroporation. Methods Enzymol 1994;235:375-85.

70. Chiti F, Dobson CM. Amyloid formation by globular proteins under native conditions. Nat Chem Biol 2009;5(1):15-22.

71. Rodriguez JA, Valentine JS, Eggers DK, Roe JA, Tiwari A, Brown RH, Jr., Hayward LJ. Familial amyotrophic lateral sclerosis-associated mutations decrease the thermal stability of distinctly metallated species of human copper/zinc superoxide dismutase. J Biol Chem 2002;277(18):15932-7.

72. Rumfeldt JA, Stathopulos PB, Chakrabarrty A, Lepock JR, Meiering EM. Mechanism and thermodynamics of guanidinium chloride-induced denaturation of ALS-associated mutant Cu,Zn superoxide dismutases. J Mol Biol 2006;355(1):106-23.

73. Stathopulos PB, Rumfeldt JA, Scholz GA, Irani RA, Frey HE, Hallewell RA, Lepock JR, Meiering EM. Cu/Zn superoxide dismutase mutants associated with amyotrophic lateral sclerosis show enhanced formation of aggregates in vitro. Proc Natl Acad Sci U S A 2003;100(12):7021-6.

74. Bruns CK, Kopito RR. Impaired post-translational folding of familial ALS-linked Cu, Zn superoxide dismutase mutants. Embo J 2007;26(3):855-66.

75. Sturtevant JM. Biochemical Applications of Differential Scanning Calorimetry. Annual Review of Physical Chemistry 1987;38:463-488.

76. Freire E. Thermal denaturation methods in the study of protein folding. Methods Enzymol 1995;259:144-68.

77. Stathopulos PB, University of Waterloo. Dept. of Biology. Stability and aggregation of amyotrophic lateral sclerosis-associated mutant copper, zinc superoxide dismutases [Thesis Ph D --University of Waterloo 2005]. Waterloo, Ont.: University of Waterloo; 2005. xxiii, 354 leaves p.

78. Vassall KA, Stathopulos PB, Rumfeldt JA, Lepock JR, Meiering EM. Equilibrium thermodynamic analysis of amyotrophic lateral sclerosis-associated mutant apo Cu,Zn superoxide dismutases. Biochemistry 2006;45(23):7366-79.

79. Vassall KA. Folding and stability studies on amyotrophic lateral sclerosis-associated Cu, Zn apo superoxide dismutases [Ph. D.]. Waterloo: University of Waterloo; 2009.

80. Natvig DO, Imlay K, Touati D, Hallewell RA. Human copper-zinc superoxide dismutase complements superoxide dismutase-deficient Escherichia coli mutants. J Biol Chem 1987;262(30):14697-701.

81. Liochev SI, Chen LL, Hallewell RA, Fridovich I. The familial amyotrophic lateral sclerosis-associated amino acid substitutions E100G, G93A, and G93R do not influence the rate of inactivation of copper- and zinc-containing superoxide dismutase by H2O2. Arch Biochem Biophys 1998;352(2):237-9.

82. Lowry OH, Rosebrough NJ, Farr AL, Randall RJ. Protein measurement with the Folin phenol reagent. J Biol Chem 1951;193(1):265-75.

83. Marklund S, Marklund G. Involvement of the superoxide anion radical in the autoxidation of pyrogallol and a convenient assay for superoxide dismutase. Eur J Biochem 1974;47(3):469-74.

84. Taylor JR. An introduction to error analysis : the study of uncertainties in physical measurements. Mill Valley, Calif.: University Science Books; 1982. x, 270 p. p.

85. Liu Y, Sturtevant JM. The observed change in heat capacity accompanying the thermal unfolding of proteins depends on the composition of the solution and on the method employed to change the temperature of unfolding. Biochemistry 1996;35(9):3059-62.

86. Doucette PA. Biophysical studies of human copper-zinc superoxide dismutase and mutants associated with the neurodegenerative disease amyotrophic lateral sclerosis [Ph.D.]: University of California, Los Angeles, United States; 2004.

87. Sandelin E, Nordlund A, Andersen PM, Marklund SSL, Oliveberg M. Amyotrophic lateral sclerosis-associated copper/zinc superoxide dismutase mutations preferentially reduce the repulsive charge of the proteins. Journal of Biological Chemistry 2007;282(29):21230-21236.

88. Calamai M, Tartaglia GG, Vendruscolo M, Chiti F, Dobson CM. Mutational analysis of the aggregation-prone and disaggregation-prone regions of acylphosphatase. J Mol Biol 2009;387(4):965-74.

89. Shaw BF, Valentine JS. How do ALS-associated mutations in superoxide dismutase 1 promote aggregation of the protein? Trends Biochem Sci 2007;32(2):78-85.

90. Banci L, Bertini I, Durazo A, Girotto S, Gralla EB, Martinelli M, Valentine JS, Vieru M, Whitelegge JP. Metal-free superoxide dismutase forms soluble oligomers under physiological conditions: a possible general mechanism for familial ALS. Proc Natl Acad Sci U S A 2007;104(27):11263-7.

91. Chattopadhyay M, Durazo A, Sohn SH, Strong CD, Gralla EB, Whitelegge JP, Valentine JS. Initiation and elongation in fibrillation of ALS-linked superoxide dismutase. Proc Natl Acad Sci U S A 2008;105(48):18663-8.

92. Rodriguez JA, Shaw BF, Durazo A, Sohn SH, Doucette PA, Nersissian AM, Faull KF, Eggers DK, Tiwari A, Hayward LJ and others. Destabilization of apoprotein is insufficient to explain Cu,Zn-superoxide dismutase-linked ALS pathogenesis. Proc Natl Acad Sci U S A 2005;102(30):10516-21.

93.   Rakhit R, Cunningham P, Furtos-Matei A, Dahan S, Qi XF, Crow JP, Cashman NR, Kondejewski LH, Chakrabartty A. Oxidation-induced misfolding and aggregation of superoxide dismutase and its implications for amyotrophic lateral sclerosis. J Biol Chem 2002;277(49):47551-6.

94.   Banci L, Bertini I, D'Amelio N, Gaggelli E, Libralesso E, Matecko I, Turano P, Valentine JS. Fully metallated S134N Cu,Zn-superoxide dismutase displays abnormal mobility and intermolecular contacts in solution. J Biol Chem 2005;280(43):35815-21.

95.   Elam JS, Taylor AB, Strange R, Antonyuk S, Doucette PA, Rodriguez JA, Hasnain SS, Hayward LJ, Valentine JS, Yeates TO and others. Amyloid-like filaments and water-filled nanotubes formed by SOD1 mutant proteins linked to familial ALS. Nat Struct Biol 2003;10(6):461-7.

96.   Bruijn LI, Becher MW, Lee MK, Anderson KL, Jenkins NA, Copeland NG, Sisodia SS, Rothstein JD, Borchelt DR, Price DL and others. ALS-linked SOD1 mutant G85R mediates damage to astrocytes and promotes rapidly progressive disease with SOD1-containing inclusions. Neuron 1997;18(2):327-38.

97.   Wang J, Xu G, Borchelt DR. High molecular weight complexes of mutant superoxide dismutase 1: age-dependent and tissue-specific accumulation. Neurobiol Dis 2002;9(2):139-48.

98.   Mahler HC, Friess W, Grauschopf U, Kiese S. Protein aggregation: pathways, induction factors and analysis. J Pharm Sci 2009;98(9):2909-34.

99.   Weiss WFt, Young TM, Roberts CJ. Principles, approaches, and challenges for predicting protein aggregation rates and shelf life. J Pharm Sci 2009;98(4):1246-77.

100.   Rakhit R, Crow JP, Lepock JR, Kondejewski LH, Cashman NR, Chakrabartty A. Monomeric Cu,Zn-superoxide dismutase is a common misfolding intermediate in the oxidation models of sporadic and familial amyotrophic lateral sclerosis. J Biol Chem 2004;279(15):15499-504.

101.   Koppel DE. Analysis of macromolecular polydispersity in intensity correlation spectroscopy: The method of cumulants. J Chem Phys 1972:574818-20.

102.   Provencher SW. CONTIN: A general purpose constrained regularization program for inverting noisy linear algebraic and integral equations. Comput Phys Commun 1982:27201-9.

103.   Jarrett JT, Lansbury PT, Jr. Seeding "one-dimensional crystallization" of amyloid: a pathogenic mechanism in Alzheimer's disease and scrapie? Cell 1993;73(6):1055-8.

104.   Ferrone F. Analysis of protein aggregation kinetics. Methods Enzymol 1999;309:256-74.

105.   Nielsen L, Khurana R, Coats A, Frokjaer S, Brange J, Vyas S, Uversky VN, Fink AL. Effect of environmental factors on the kinetics of insulin fibril formation: elucidation of the molecular mechanism. Biochemistry 2001;40(20):6036-46.

106.   Maa YF, Hsu CC. Investigation on fouling mechanisms for recombinant human growth hormone sterile filtration. J Pharm Sci 1998;87(7):808-12.

107.   Maa YF, Hsu CC. Protein denaturation by combined effect of shear and air-liquid interface. Biotechnol Bioeng 1997;54(6):503-12.

108.   Bowling AC, Barkowski EE, McKenna-Yasek D, Sapp P, Horvitz HR, Beal MF, Brown RH, Jr. Superoxide dismutase concentration and activity in familial amyotrophic lateral sclerosis. J Neurochem 1995;64(5):2366-9.

109. Kurobe N, Suzuki F, Okajima K, Kato K. Sensitive enzyme immunoassay for human Cu/Zn superoxide dismutase. Clin Chim Acta 1990;187(1):11-20.

110. Pardo CA, Xu Z, Borchelt DR, Price DL, Sisodia SS, Cleveland DW. Superoxide dismutase is an abundant component in cell bodies, dendrites, and axons of motor neurons and in a subset of other neurons. Proc Natl Acad Sci U S A 1995;92(4):954-8.

111. Kiese S, Papppenberger A, Friess W, Mahler HC. Shaken, not stirred: mechanical stress testing of an IgG1 antibody. J Pharm Sci 2008;97(10):4347-66.

112. Goda S, Takano K, Yamagata Y, Nagata R, Akutsu H, Maki S, Namba K, Yutani K. Amyloid protofilament formation of hen egg lysozyme in highly concentrated ethanol solution. Protein Sci 2000;9(2):369-75.

113. Murali J, Koteeswari D, Rifkind JM, Jayakumar R. Amyloid insulin interaction with erythrocytes. Biochem Cell Biol 2003;81(1):51-9.

114. Pallitto MM, Ghanta J, Heinzelman P, Kiessling LL, Murphy RM. Recognition sequence design for peptidyl modulators of beta-amyloid aggregation and toxicity. Biochemistry 1999;38(12):3570-8.

115. Wu C, Biancalana M, Koide S, Shea JE. Binding modes of thioflavin-T to the single-layer beta-sheet of the peptide self-assembly mimics. J Mol Biol 2009;394(4):627-33.

116. Kato S, Nakashima K, Horiuchi S, Nagai R, Cleveland DW, Liu J, Hirano A, Takikawa M, Kato M, Nakano I and others. Formation of advanced glycation end-product-modified superoxide dismutase-1 (SOD1) is one of the mechanisms responsible for inclusions common to familial amyotrophic lateral sclerosis patients with SOD1 gene mutation, and transgenic mice expressing human SOD1 gene mutation. Neuropathology 2001;21(1):67-81.

117. Hou X, Aguilar MI, Small DH. Transthyretin and familial amyloidotic polyneuropathy. Recent progress in understanding the molecular mechanism of neurodegeneration. Febs J 2007;274(7):1637-50.

118. Nielsen L, Frokjaer S, Brange J, Uversky VN, Fink AL. Probing the mechanism of insulin fibril formation with insulin mutants. Biochemistry 2001;40(28):8397-409.

119. Rakhit R, Robertson J, Vande Velde C, Horne P, Ruth DM, Griffin J, Cleveland DW, Cashman NR, Chakrabartty A. An immunological epitope selective for pathological monomer-misfolded SOD1 in ALS. Nat Med 2007;13(6):754-9.

120. Lee S, Fernandez EJ, Good TA. Role of aggregation conditions in structure, stability, and toxicity of intermediates in the Abeta fibril formation pathway. Protein Sci 2007;16(4):723-32.